Shear stabilization of a solidifying front: Weakly nonlinear analysis in a long-wave limit

T. P. Schulze

Department of Applied Mathematics and Theoretical Physics, University of Cambridge, Silver Street, Cambridge CB3 9EW, England

S. H. Davis

Department of Engineering Sciences and Applied Mathematics, Northwestern University, Evanston, Illinois 60208

The manufacturing of single crystals of multi-component materials with uniform material properties is frequently hampered by the presence of morphological instabilities during the solidification. In this paper we extend into the nonlinear regime our previous work on the influence of shear flows on the linear stability of the solid/liquid interface during the directional solidification of binary alloys. The flows are generated by unidirectional or nonplanar harmonic oscillations of the crystal parallel to the mean interface position, and oscillations with physically realizable amplitudes and frequencies are found to be useful for stabilization purposes. A strongly nonlinear equation which governs the evolution of the interface in the limit of high surface energy, a weak flow and thermodynamic equilibrium is derived, and a weakly nonlinear analysis of this equation is performed. For the unidirectional case, it is found that oscillations with sufficiently large amplitude will change the initial bifurcation from super- to subcritical. For the nonplanar case, it is found that subcritical instability of roll, square and hexagonal cells is favored as the amplitude of the flow is increased. Thus, some of the stabilization due to the flow may be lost at finite amplitude, but substantial stabilization can be retained. © *1996 American Institute of Physics.* [S1070-6631(96)01509-7]

I. INTRODUCTION

Phase changes are intimately involved in the manufacturing and processing of nearly all materials. The control of fluid motion and interfaces during these processes is essential to the production of quality materials. Among the greater threats to material quality are hydrodynamic and interfacial instabilities, which may lead to nonuniform material properties. Here, we shall focus on the liquid-to-solid phase transformation of two-component alloys. The study of crystalline solids with binary composition is of particular interest, since many technologically significant materials—including metallic alloys, semiconductor materials and crystals for optical devices—fall into this category.

Directional solidification is a processing configuration which lends itself to experimental observation and mathematical analysis, and is a good local model for other complex solidification configurations, such as laser annealing. In a directional solidification experiment, a liquid may be confined to a Hele-Shaw cell (Figure 1) or to a fully three-dimensional region (inside a cylindrical tube, for example). The confined material, along with its container, is then pulled through a temperature gradient, so that the fluid solidifies as it moves from a heated region into a cooler one. If the material is pulled at constant speed, the solid-liquid interface will establish itself at a fixed position relative to the heat source and/or sink.

The melting temperature of the fluid, and hence the interfacial temperature, is related to the concentration of the alloy and to the curvature of the interface. These two effects are governed by the Gibbs-Thompson equation:

$$T_I = T_M - 2\frac{T_M H \gamma}{L_V} + mC,\tag{1}$$

which gives the interfacial temperature T_I as a function of the concentration of the alloy C and the mean curvature H of the interface. The other symbols in this equation represent the melting temperature of the pure material T_M, the surface energy per unit area γ, the liquidus slope in the phase diagram of the binary alloy m, and the latent heat per unit volume released upon solidification L_V. In applying this equation we assume that the interface is moving slowly enough that the system remains in thermodynamic equilibrium. Thus, the effects of kinetic undercooling, which would lower the interface temperature as the pulling speed is increased, are ignored.

The instability of the planar front was first explained by Tiller *et al.*[1] and a full linear-stability analysis, including the effects of surface energy, was first done by Mullins and Sekerka.[2] They found that the interface is stable for sufficiently low solute concentrations. For higher concentrations, the interface is unstable for a finite range of pulling speeds. Near the critical values of the pulling speed, the linear theory predicts the formation of sinusoidal cells.

The mechanism can be explained by examining the fate of a small perturbation to the interface. A bump of solid will put the front in a higher temperature environment, and tends to be melted back; thus, the temperature distribution is stabilizing. A bump of solid has its local melting temperature decreased by the Gibbs-Thompson effect (capillary undercooling); surface energy is stabilizing. A bump of solid will protrude into a region of reduced solute concentration due to
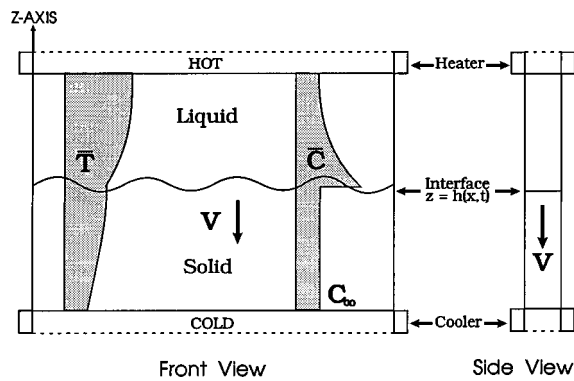
FIG. 1. Configuration for directional solidification in a Hele-Shaw cell. The confined material is pulled through a temperature gradient, so that the fluid solidifies as it moves from a heated region into a cooler one. If the material is pulled at constant speed, the solid-liquid interface will establish itself at a fixed position relative to the heat source and/or sink.

the effects of solute rejection, which elevates the concentration of solute in a layer near the interface. Thus, the local melting temperature near a bump will be reduced due to constitutional undercooling and continued growth will be favored. This last effect can be related to the (negative) concentration gradient at the interface G_C, with larger values of $|G_C|$ indicating a greater tendency for interfacial instability.

When the instability is present, variations in the concentration along the interface are frozen into the solid, resulting in stripes of elevated solute concentration. Frequently, these inhomogeneities are undesirable, and crystal growers would prefer to suppress the instability. A number of authors have attempted to use a forced fluid flow to extend the range of

pulling speeds for which the interface remains flat (see Davis[3] for a summary of these). Schulze and Davis[4,5] have investigated the effects of translating the crystal in elliptical orbits parallel to the interface, following the example of Kelly and Hu,[6] who had found that a similar modulation has a stabilizing influence on Bénard convection. This nonplanar forcing will generate a three-dimensional version of a Stokes boundary layer in the fluid above the interface. Because the boundary layer will be compressed due to the flow normal to the interface generated by the pulling of the crystal, we refer to this flow configuration as a three-dimensional Compressed Stokes Layer (3D CSL), or CSL for short.

Schulze and Davis[5] found that this flow can, on a linear theory basis, stabilize the interface, provided the pulling speed is sufficiently high. The success of this method requires that the frequency of the flow lie within a calculated range. The outermost curve in Figure 2 is a typical neutral curve for the no-flow system,[2] showing the critical pulling speed as a function of the alloy concentration for a fixed temperature gradient. Also shown in this figure are neutral curves for the system when it is forced through the boundary to generate a CSL. As the amplitude of the forcing is increased, the upper branch of the neutral curve is lowered considerably and the nose of the curve moves to the right, so that, according to linear theory, the system is stabilized relative to the no-flow case. While it is true that most practical solidification occurs at low speeds (i.e., along the lower branch of the neutral curve), some applications make use of ''rapid'' directional solidification. [An example of this is laser annealing, in which a high-powered laser is scanned across a solid substrate. This causes the local melting of the
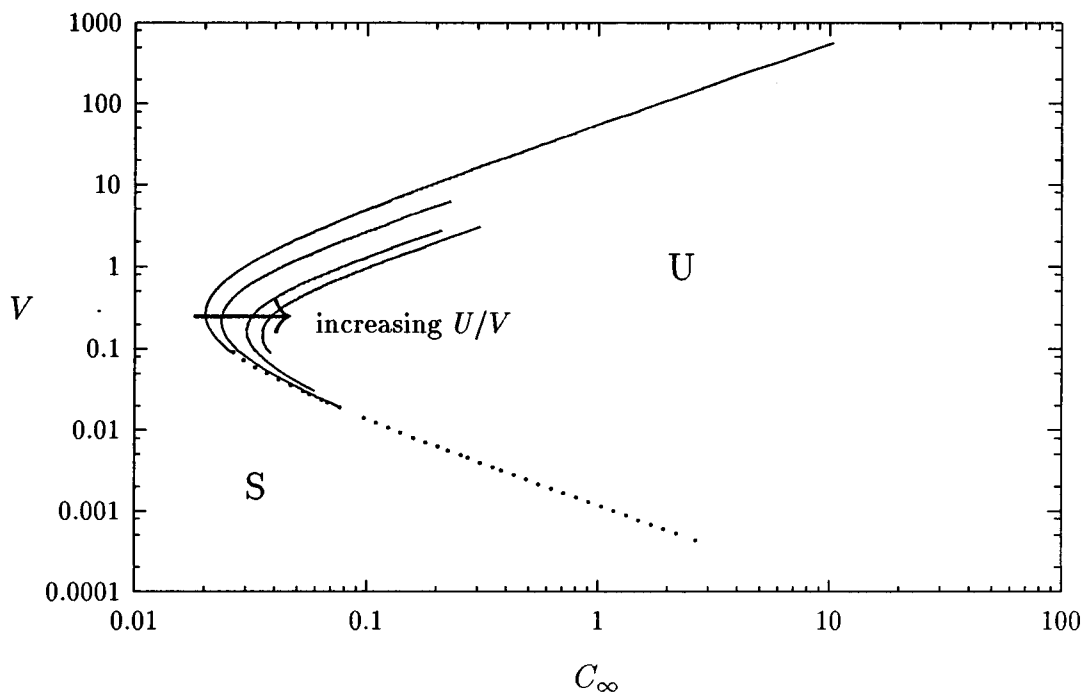

FIG. 2. Plot of a typical neutral curve in dimensional form—V versus C_∞ with a fixed temperature gradient. All of the curves extend infinitely along tangents to the portions shown. The interface is linearly stable (S) when the far-field concentration is to the left of the neutral curve. The no-flow (outermost) curve is divided into a portion corresponding to subcritical instability (dashed portion) and a portion corresponding to supercritical instability (solid portion).

                                          T. P. Schulze and S. H. Davis

solid and rapid resolidification (1–10 m/s) after the laser passes.[14] At such high speeds one's model should allow departures from local thermodynamic equilibrium[15–18] though in the present analysis such effects are not considered.] Furthermore, the stabilization produced by the CSL may allow more applications to operate above the neutral curve. In general, it is desirable to solidify as quickly as possible to limit laboratory noise, such as fluctuations in the temperature gradient, and to enhance production rates in industrial applications. Finally, even low-speed applications will benefit by moving the nose of the neutral curve to the right. This shift is a factor of two for the case shown in Figure 2, which corresponds to a lead tin alloy. Materials which reject more solute will have larger shifts.

For a pulling speed near the nose of the neutral curve, typical values for the frequency and amplitude of the lateral velocity oscillations which lead to stabilization of the interface are 10^4 Hz and 10^{-3} cm, respectively. Such scales would lend themselves well to an acoustic forcing. The precise value of these parameters can vary over several orders of magnitude, but, as a rule, vary with the solute-diffusion length and time scales and are physically realizable for a sizable range of operating conditions.

A weakly nonlinear analysis of the no-flow, two-dimensional system was first done by Wollkind and Segel.[7] Their analysis revealed that bifurcations are generally subcritical for low pulling velocities, and supercritical at higher velocities, as shown in Figure 2. Notice that the bifurcations for the no-flow system are supercritical precisely where the CSL flow provides effective stabilization.

In this paper the effect of the CSL on the bifurcation structure for morphological instability will be investigated. Our principal aim is to discover under what conditions the flow may provide effective control of interfacial instability. Of particular concern is the possibility that subcritical instabilities could reduce, or even eliminate, the stabilization indicated by the linear theory. When the interface is unstable, there are the usual variety of potential patterns for the instability to take, including square, hexagonal and two-dimensional (roll) cells, and we shall discuss the use of this flow as a pattern-selection mechanism.

Our focus will be the upper branch of the curve shown in Figure 2, for it is in this region that the CSL has a strong influence on the interfacial morphology. Along this portion of the neutral curve the critical wavelength of interfacial disturbances is long compared to the solutal boundary-layer thickness, and an analysis which exploits this fact will be used. The principal advantage of a long-wave limit is that it greatly simplifies the governing equations, allowing one to solve for the interface shape without knowing the details of the bulk fields.

Considering the limit of the small segregation coefficient, Sivashinsky[8] was the first to derive a long-wave evolution equation for a directionally solidifying interface. Other distinguished limits leading to long-wave evolution equations in the absence of flow were discussed by Riley and Davis.[9] Here we shall follow the work of Brattkus and Davis[10] (BD), who derived and analyzed a long-wave evolution equation valid near the upper branch of the neutral curve

shown in Figure 2. In this limit, which is called the absolute stability limit, they found that bifurcations to two-dimensional, parallel cells are always supercritical, and that, in some cases, there are linearly stable, three-dimensional hexagonal solutions. The last result is possible because their equation features both quadratic and cubic nonlinearities:

$$h_{TT} - \left(2 + \frac{1}{k}\right)\nabla^2 h_T + \left(1 + \frac{1}{k}\right)\nabla^4 h + k\nabla^2 h + k\mathscr{M}^{-1}h$$

$$= h_T \nabla^2 h + |\nabla h|_T^2 - \nabla^2 |\nabla h|^2 - \frac{1}{k}\nabla \cdot (\nabla^2 h \nabla h)$$

$$- \frac{1}{2}\nabla \cdot (\nabla h |\nabla h|^2), \tag{2}$$

where $z = h(X, Y, T)$ gives the leading-order interface deflection, the extent to which solute is rejected is measured by the segregation coefficient k, $\mathscr{M}$ is a rescaled morphological number, ∇ is the Laplacian and the dependent variables X, Y and T are all on long or slow scales. In order to simplify the presentation of modified versions of this equation we shall abbreviate the linear and nonlinear operators shown above by L and N, respectively, so that the equation may be written symbolically as

$$L[h] = N[h]. \tag{3}$$

Equation (2) has been the starting point for several recent studies. Hobbs and Metzener[11] derived a linear correction to the equation for solidification into a flow with the asymptotic suction profile (ASP). They found that the interface is given by a traveling wave whose amplitude depends on slower scales in time and space. In Sections II and III we give the derivation of an analogous equation for the case of solidification into a 3D CSL.

Using both numerical and analytic techniques, Kassner et al.[12] studied a two-dimensional version of (2), including diffusion in the solid as well as the liquid. They examined secondary bifurcations, including the Eckhaus instability, parity-breaking, vacillating-breathing and period-halving bifurcations. In a second paper they examined the transition to chaos via quasiperiodic states.[13]

Skeldon et al.[23] have done a numerical study of the entire class of long-wave equations identified by Riley and Davis,[9] including the Brattkus-Davis equation. They find new bifurcation points, new solution branches and the existence of inverted hexagonal nodes and cells.

Hoyle, McFadden and Davis[19] derived corrections to equation (2) when the surface tension is anisotropic. Depending on the direction of the growth with respect to the crystal lattice, they find that the anisotropy may affect the linear, quadratic or cubic terms in the evolution equation. Using their modified equation, they derive amplitude equations governing the weakly nonlinear growth and competition of two-dimensional, rectangular and hexagonal cells.

In Section II the governing equations are presented and manipulated into a form that is convenient for the subsequent analysis. In Section III a correction to equation (2) is derived for solidification into a CSL. In Sections IV and V amplitude equations are derived from the evolution equation

that governs the development of (2D) cells and cells, squares and hexagons in three dimensions. In Section VI our results are summarized.

II. GOVERNING EQUATIONS

We consider the directional solidification of a dilute binary mixture at constant speed V. We choose a coordinate system with the x-y-plane located at the mean position of the crystal interface. Our frame of reference moves with the crystal, so that the solidified crystal appears stationary to a viewer in this frame, and the fluid in the far-field appears to undergo elliptical oscillations parallel to the interface.

The equations governing the system in the fluid region are the Navier-Stokes, continuity and solute-diffusion equations. The Navier-Stokes equations contain a time-periodic forcing term due to the non-Galilean transformation that moves us into the frame of reference of the crystal. The system is assumed to be in thermodynamic equilibrium at all times. To further simplify the analysis, we neglect latent heat and density changes, and assume equal densities and thermal properties between the two phases. We also assume that heat diffuses much faster than the solute, and, in this limit, the temperature field is fixed and depends linearly on the coordinate normal to the interface (the frozen-temperature approximation[20]). We find it convenient to write separate equations for the tangential velocity components $\mathbf{u} = u\mathbf{i} + v\mathbf{j}$ and the normal component w. Note that gravity is absent in this model. In nondimensional form, the equations are

$$\Omega \mathbf{u}_t + R(\mathbf{u}\cdot\nabla\mathbf{u} + w\mathbf{u}_z) - \mathbf{u}_z = -\nabla p + S\nabla^2\mathbf{u} + \Omega\mathbf{U}_t, \quad (4a)$$

$$\Omega w_t + R(\mathbf{u}\cdot\nabla w + ww_z) - w_z = -p_z + Sw_{zz}, \quad (4b)$$

$$\nabla\cdot\mathbf{u} + w_z = 0, \quad (4c)$$

$$\Omega C_t + R(\mathbf{u}\cdot\nabla C + wC_z) - C_z = \nabla^2 C, \quad (4d)$$

$$T = z, \quad (4e)$$

where

$$\mathbf{U} = \cos t\,\mathbf{i} + \beta\,\cos(t-\gamma)\mathbf{j} \quad (5)$$

is the velocity of the crystal with respect to the far-field, and the Laplacian, gradient and divergence operators act in the horizontal plane only. For convenience we rewrite $\mathbf{U}$ as

$$\mathbf{U} = \mathbf{r}e^{i\tau} + \text{c.c.}, \quad (6)$$

where

$$\mathbf{r} = \frac{1}{2}(\mathbf{i} + \beta e^{-i\gamma}\mathbf{j}), \quad (7)$$

and c.c. indicates the complex conjugate. The vector $\mathbf{r}$ contains the information on the orientation, size and eccentricity of the elliptical motion of the crystal in terms of the phase γ and amplitude ratio β of the two perpendicular oscillations indicated by (5).

We have nondimensionalized the equations using the following scalings:

$$\mathbf{x} \to (D/V)\mathbf{x}, \quad \mathbf{u} \to U\mathbf{u}, \quad w \to Uw, \quad p \to \rho UVp, \quad (8a)$$

$$T \to (GD/V)T + T_0, \quad C \to (C_\infty - C_\infty/k)C + C_\infty/k,$$

$$t \to t/\omega, \quad (8b)$$

where D is the solute diffusivity in the liquid, V is the crystal pulling speed, U is the amplitude of the velocity oscillations in the x-direction, ρ is the material density, C_∞ is the far-field concentration, ω is the angular frequency of the elliptical translation of the crystal, G is the thermal gradient, T_0 is the temperature of the interface in the basic state and k is the segregation coefficient.

The nondimensional parameters that appear in the equations and boundary conditions are the morphological number M, which gives the ratio of the solutal and thermal gradients at the interface, the surface energy parameter Γ, the Schmidt number S, the nondimensional angular frequency Ω, the segregation coefficient k and a ratio R measuring the amplitude of the lateral oscillations in units of pulling speed:

$$M = \frac{mVC_\infty(1-1/k)}{GD}, \quad \Gamma = \frac{T_m\gamma V}{DL_V mC_\infty(1-1/k)}, \quad (9a)$$

$$S = \frac{\nu}{D}, \quad \Omega = \frac{\omega D}{V^2}, \quad R = \frac{U}{V}. \quad (9b)$$

The far-field boundary conditions are, as $z \to \infty$,

$$\mathbf{u} \to -\mathbf{U}, \quad (10a)$$

$$w, p \to 0, \quad (10b)$$

$$C \to 1, \quad (10c)$$

and the interfacial conditions, evaluated at the interface $z = h(x,y,t)$, are

$$\mathbf{u} = w = 0, \quad (11a)$$

$$C = M^{-1}h - 2\Gamma H, \quad (11b)$$

$$[1 + \Omega h_t][1 + (k-1)C] = C_z - \nabla h\cdot\nabla C, \quad (11c)$$

where mean curvature of the interface, H, is given by

$$2H = \nabla\cdot[\nabla h(1 + |\nabla h|^2)^{-1/2}]. \quad (12)$$

Equations (11a) represent no-slip and a mass balance. Equation (11b) is a nondimensional version of the Gibbs-Thomson equation (1), and equation (11c) is a balance of solute across the interface.

The linear stability theory for this system[4,5] is tacitly summarized by Figures 2 and 3. The first of these has already been discussed. Figure 3 maps out the regions of the nondimensional frequency versus disturbance wavenumber plane where a weak CSL will stabilize or destabilize the interface relative to the case without flow. Notice that there is a finite range of frequencies for which a weak CSL stabilizes disturbances with arbitrary wavenumbers.

III. THE DERIVATION OF THE EVOLUTION EQUATION

We wish to derive a correction to the long-wave evolution equation (2), which is valid in the same limit as that used by BD. Figure 4 shows how this limit fits into the general linear theory. Here, the no-flow neutral curve shown in Figure 2 is recast in terms of nondimensional variables,
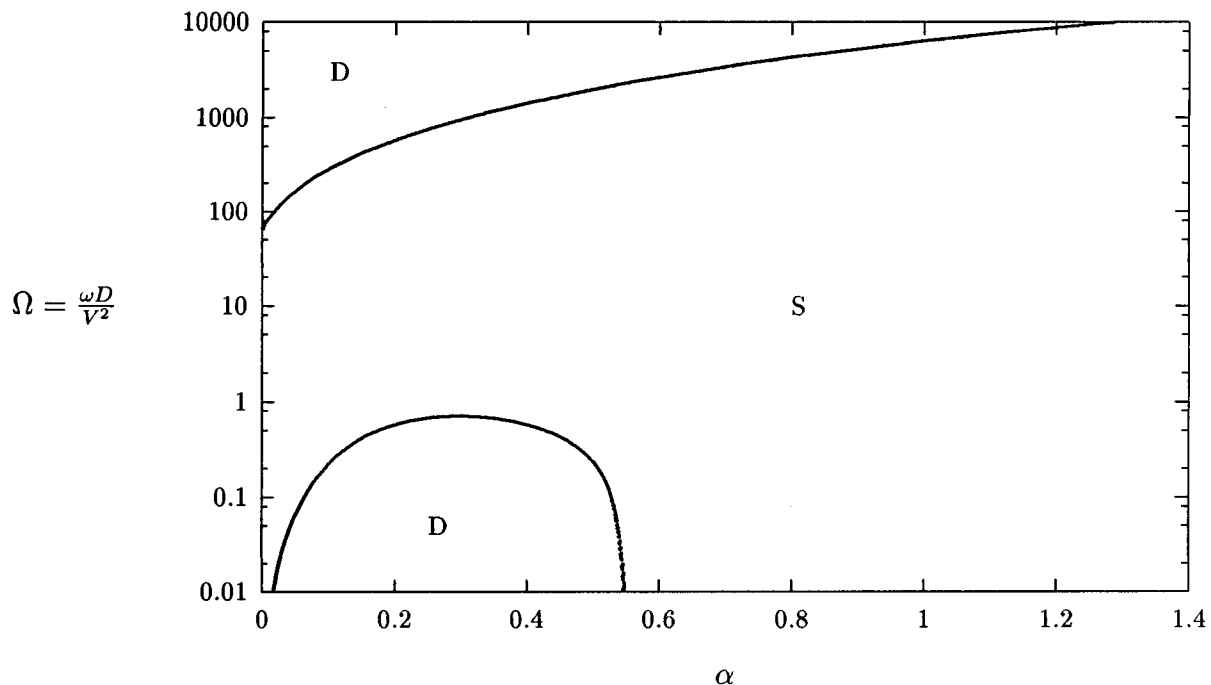
FIG. 3. Regions of the α-Ω plane where the flow stabilizes (S) or destabilizes (D) the interface relative to the case without flow.[4] $S=81.0$ and $k=0.3$; result is independent of Γ.

the inverse morphological number M^{-1} versus the surface energy parameter Γ. The system is stable (unstable) for parameter values above (below) this curve, with the wavelength of the instability approaching zero near the top of the curve and infinity near the bottom. The system is stable for all $\Gamma > \Gamma_s = 1/k$. We introduce the small parameter ϵ as a measure of closeness to this point, which is known as the absolute stability limit:
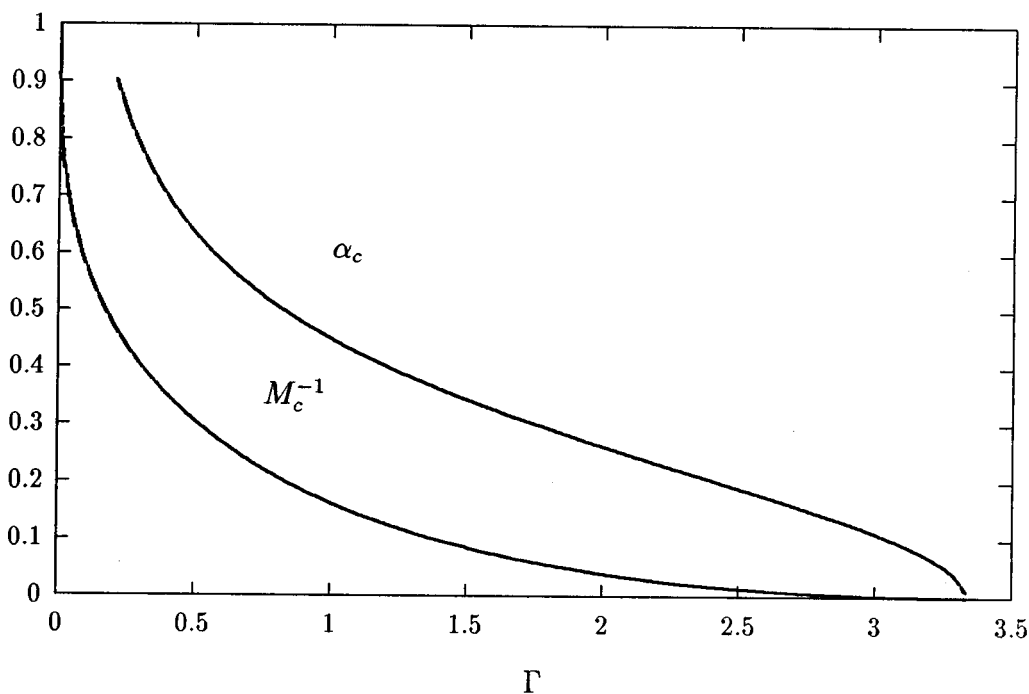

FIG. 4. The critical value (maximized over wavenumbers) of M^{-1} and the critical wavenumber as a function of Γ for $k=0.3$. Stable and unstable regions lie above and below the M_c^{-1}-versus-Γ curve, respectively. The absolute stability limit is $\Gamma_s = 1/k$.

$$\epsilon^4 = 1/k - \Gamma. \tag{13}$$

In this limit, the system becomes linearly unstable to long-wave disturbances when the morphological number becomes very large. In terms of physical variables, this limit can be thought of as large pulling speed or small far-field concentration.

The linear stability theory suggests the following slow space and time scales:

$$X = \epsilon^2 x, \quad Y = \epsilon^2 y, \quad T = \epsilon^4 t. \tag{14}$$

Near the absolute stability limit, the morphological number scales like

$$\mathscr{M} \sim \epsilon^8 M, \tag{15}$$

with $\mathscr{M} \sim O(1)$.

These are equivalent to the scalings employed by both BD and Hobbs and Metzener.[11] Our definition of ϵ is related to those of these previous authors by a power of $1/4$ and $1/2$, respectively.

Hobbs and Metzener examined the limit $S \sim O(\epsilon^{-4})$, $R \sim O(1)$, and note that, for their problem, the results are similar to the limit $S \sim O(1)$, $R \sim O(\epsilon^4)$. We refer to these as the large Schmidt number and weak-flow limits, respectively. We expect that the two limits produce qualitatively similar results for our problem as well, and we choose to consider the weak-flow case. In order to obtain a distinguished limit where we can derive an $O(1)$ correction to equation (2), we find that we have to take a finer scaling of the velocity ratio R than was necessary for the steady shear flow. The appropriate scaling turns out to be

$$R = \epsilon \mathscr{R}, \tag{16}$$

with $\mathscr{R} \sim O(1)$.

The analogous scaling for the ASP is $R = \epsilon^2 \mathscr{R}$. This scaling produces no correction to equation (2) at leading order when used for the CSL, indicating that the CSL has, in some sense, a weaker influence on the interface for a given flow amplitude. If the ASP-scaling were used with the CSL flow, the flow terms that appear at the same order as the evolution equation would be time-periodic, and their effect would average out of the equation when a solvability condition was applied. By making the flow somewhat stronger these unsteady terms appear earlier in the analysis and steady terms ultimately emerge from products of the lower-order time-periodic terms. If the flow were $O(1)$, however, the need for a solvability condition would arise too early, resulting in a flow-dominated evolution equation with the result of BD as a weak correction.

For the CSL, it is necessary to retain a fast time scale in addition to the slow scale presented earlier. We denote this new scale as $\tau = t$, and employ a multiple-scale analysis in time.

In order to simplify the derivation of the evolution equation, we use the standard technique of changing variables so that the interfacial conditions may be applied at zero rather than at the interface position $z = h(X, Y, T, \tau)$:

$$\zeta = z - h(X, Y, T, \tau). \tag{17}$$

If all of the changes outlined above are taken into account, the governing equations become

$$\Omega[\mathbf{u}_\tau + \mathbf{U}_\tau - h_\tau \mathbf{u}_\zeta + \epsilon^4(\mathbf{u}_T - h_T \mathbf{u}_\zeta)] + \epsilon^3 \mathscr{R}[(\mathbf{u} \cdot \nabla)\mathbf{u}$$
$$- (\mathbf{u} \cdot \nabla h)\mathbf{u}_\zeta] + \epsilon \mathscr{R} w \mathbf{u}_\zeta + \epsilon^2(\nabla p - \nabla h p_\zeta)$$
$$= S\mathbf{u}_{\zeta\zeta} + \mathbf{u}_\zeta + \epsilon^4 S[\nabla^2 \mathbf{u} - 2(\nabla h \cdot \nabla)\mathbf{u}_\zeta$$
$$- \nabla^2 h \mathbf{u}_\zeta + |\nabla h|^2 \mathbf{u}_{\zeta\zeta}], \tag{18a}$$

$$\Omega[w_\tau - h_\tau w_\zeta + \epsilon^4(w_T - h_T w_\zeta)] + \epsilon^3 \mathscr{R}[(\mathbf{u} \cdot \nabla)w$$
$$- (\mathbf{u} \cdot \nabla h)w_\zeta] + \epsilon \mathscr{R} w w_\zeta + p_\zeta$$
$$= S w_{\zeta\zeta} + w_\zeta + \epsilon^4 S[\nabla^2 w - 2(\nabla h \cdot \nabla)w_\zeta$$
$$- \nabla^2 h w_\zeta + |\nabla h|^2 w_{\zeta\zeta}], \tag{18b}$$

$$w_\zeta + \epsilon^2(\nabla \cdot \mathbf{u} - \nabla h \cdot \mathbf{u}_\zeta) = 0, \tag{18c}$$

$$\Omega[C_\tau - h_\tau C_\zeta + \epsilon^4(C_T - h_T C_\zeta)] + \epsilon^3 \mathscr{R}[(\mathbf{u} \cdot \nabla)C$$
$$- (\mathbf{u} \cdot \nabla h)C_\zeta] + \epsilon \mathscr{R} w C_\zeta$$
$$= C_{\zeta\zeta} + C_\zeta + \epsilon^4 S[\nabla^2 C - 2(\nabla h \cdot \nabla)C_\zeta$$
$$- \nabla^2 h C_\zeta + |\nabla h|^2 C_{\zeta\zeta}]. \tag{18d}$$

The far-field boundary conditions remain the same, and the interfacial conditions are now applied at $\zeta = 0$:

$$\mathbf{u} = w = 0, \tag{19a}$$

$$C = \epsilon^8 \mathscr{M}^{-1} h - (1/k - \epsilon^4)\epsilon^4 \nabla \cdot [\nabla h(1 + \epsilon^4 |\nabla h|^2)^{-1/2}], \tag{19b}$$

$$C_\zeta = [1 + \Omega(h_\tau + \epsilon^4 h_T)][1 + (k-1)C]$$
$$+ \epsilon^4(\nabla h \cdot \nabla C - |\nabla h|^2 C_\zeta). \tag{19c}$$

To derive the evolution equation, we expand each dependent variables in powers of the small parameter ϵ:

$$\mathbf{u} = \mathbf{u}_0 + \epsilon \mathbf{u} + \dots, \tag{20a}$$

$$w = w_0 + \epsilon w_1 + \dots, \tag{20b}$$

$$h = h_0 + \epsilon h_1 + \dots, \tag{20c}$$

$$C = C_0 + \epsilon C_1 + \dots, \tag{20d}$$

and solve the resulting equations at each order. The lower-order solutions are given in the Appendix (see Schulze[22] for further details). At $O(\epsilon^8)$ only the steady portion of the solute diffusion equation is required:

$$\bar{C}_{8\zeta\zeta} + \bar{C}_{8\zeta} = \Omega(C_{4T} - h_{0T}C_{4\zeta}) - \nabla^2 C_4 + \nabla^2 h_0 C_{4\zeta}$$
$$- |\nabla h_0|^2 C_{4\zeta\zeta} + 2\nabla h_0 \cdot \nabla C_{4\zeta}$$
$$+ \mathscr{R}\left[\overline{(\mathbf{u}_0 \cdot \nabla)C_5} - C_{0\zeta}\int_0^\zeta \nabla \cdot \bar{\mathbf{u}}_5 d\zeta\right], \tag{21}$$

where the overbars indicate averages over one period in the fast time τ. The boundary conditions are

T. P. Schulze and S. H. Davis

$$\overline{C}_8 = \mathcal{M}^{-1}h_0 + \frac{1}{2k}\nabla\cdot(\nabla h_0|\nabla h_0|^2) + \nabla^2 h_0, \quad \text{at} \ \zeta=0,$$
$$(22a)$$

$$\overline{C}_{8\zeta} + (1-k)\overline{C}_8 = \Omega(k-1)C_4 h_{0T} - C_{4\zeta}|\nabla h_0|^2$$
$$+ \nabla C_4 \cdot \nabla h_0, \quad \text{at} \ \zeta=0, \qquad (22b)$$

$$\overline{C}_8 = 0, \quad \text{as} \ \zeta\to\infty. \qquad (22c)$$

Here, the third boundary condition on the second-order equation (21) plays the roll of a solvability condition, and this determines the evolution equation for $h_0(X,Y,T)$:

$$L[h_0] + \mathcal{R}^2 f_0 \nabla^2 |\mathbf{r}\cdot\nabla|^2 \mathcal{F}^{-1}\left[\frac{\hat{h}_0}{|\mathbf{k}|}\right] = N[h_0]. \qquad (23)$$

The operators L and N are defined by equation (3) and the symbol $\mathcal{F}^{-1}$ indicates the inverse of a double Fourier transform in the slow scales X and Y:

$$\mathcal{F}[\phi(X,Y,T,\tau,\eta)] = \hat{\phi}(k_1,k_2,T,\tau,\eta)$$
$$= \frac{1}{2\pi}\int_{-\infty}^{\infty}\int_{-\infty}^{\infty}\phi e^{i\mathbf{k}\cdot\mathbf{X}}dXdY, \qquad (24)$$

where $\mathbf{k}=(k_1,k_2)$ and $\mathbf{X}=(X,Y)$. The coefficient f_0 is a function of S and Ω, and its explicit form may be found in the Appendix.

The left-hand side of the evolution equation is a fourth-order spatial, second-order temporal linear operator that differs from the operator in equation (2) by the presence of the flow term, which is proportional to the square of the velocity ratio $\mathcal{R}$. Note that the correction due to the flow is linear. For the purpose of performing a weakly nonlinear analysis the form of this term may therefore be obtained from the characteristic equation of the linear stability theory. However, equation (23) is also valid for strongly nonlinear disturbances and, in general, can not be arrived at in this manner due to the non-local behavior implied by the Fourier transform that appears in the correction term. When solving the equation, it is necessary to invert this transform. For the weakly nonlinear analysis one need only work with functions of the form $h_0=Ae^{i\mathbf{k}_0\cdot\mathbf{X}}$ which transform to $\hat{h}_0=A\sqrt{2\pi}\delta(\mathbf{k}-\mathbf{k}_0)$. The inverse transform appearing in the evolution equation is then given by

$$\mathcal{F}^{-1}\left[\frac{\hat{h}_0}{|\mathbf{k}|}\right] = \frac{A}{|\mathbf{k}_0|}e^{i\mathbf{k}_0\cdot\mathbf{X}}, \qquad (25)$$

and one finds that the resulting flow term is consistent with the linear stability theory. We shall not pursue strongly nonlinear solutions here, but give the full equation for future reference.

For comparison, the evolution equation from Hobbs and Metzener[11] for the asymptotic suction profile is reproduced:

$$L[h_0] - Rs\,\partial_X \mathcal{F}^{-1}[|\mathbf{k}|\hat{h}_0] = N[(h_0,X,Y,T)], \qquad (26)$$

where s is a rescaled Schmidt number. The flow term for the CSL differs from that for the ASP in two ways. First, the flow term for the CSL is a more complicated function and depends on the additional flow parameter Ω. Second, the flow term for the CSL is third order in space instead of

second order, indicating a correction to the linear no-flow theory that is proportional to the cube, instead of the square, of the wavenumber. The right-hand sides of both evolution equations contain quadratic and cubic nonlinear terms, and are identical to the terms found in equation (2).

IV. TWO-DIMENSIONAL BIFURCATION THEORY

Consider the Y-independent form of the evolution equation, omitting the zero subscript on h:

$$L[h] + \frac{1}{4}\mathcal{R}^2 f_0 \mathcal{F}_{XXXX}^{-1}\left[\frac{\hat{h}}{|\alpha|}\right] = N[h]. \qquad (27)$$

We expand the function $h(X,T)$ (previously h_0) as an asymptotic series in powers of a new small parameter δ, which is related to the amplitude of an interfacial disturbance:

$$h(X,Y) = \delta h_1(X,T) + \delta^2 h_2(X,T) + \dots . \qquad (28)$$

At leading order, we get the linearized form of the evolution equation. If we seek a solution in terms of normal modes:

$$h_1(X,T) = Ae^{\sigma T + i\alpha X}, \qquad (29)$$

we obtain a long-wave version of the linear stability theory,[4] with the characteristic equation

$$\sigma^2 - \left(2+\frac{1}{k}\right)\sigma + \left(1+\frac{1}{k}\right)\alpha^4 - k\alpha^2 + \frac{1}{4}\mathcal{R}^2 f_0 \alpha^3 + k\mathcal{M}^{-1} = 0, \qquad (30)$$

for $\alpha>0$. Here the symbol for the wavenumber $k=|\mathbf{k}|$ has been replaced by α to avoid confusion with the segregation coefficient k.

Setting the real part of σ equal to zero reveals that the characteristic equation can only be satisfied if

$$\left(2+\frac{1}{k}\right)\sigma_i = 0. \qquad (31)$$

This implies that σ_i must also be zero on the neutral curve, because the coefficient $2+1/k$ is positive for all physically relevant k. This feature, which is sometimes referred to as the "principal of exchange of stabilities," was first proven for the directional solidification of a binary alloy in the absence of flow by Wollkind and Segel.[7]

The critical wavenumber, based on the long-wave theory, is given by

$$\alpha_c = \frac{-12f_0 k\mathcal{R}^2 + \sqrt{128k^2(1+k) + 9f_0^2 k^2\mathcal{R}^4}}{128(1+k)}. \qquad (32)$$

The critical morphological number is then given by

$$k\mathcal{M}_c^{-1} = k\alpha_c^2 - \left(1+\frac{1}{k}\right)\alpha_c^4 - \frac{1}{4}\mathcal{R}^2 f_0 \alpha_c^3. \qquad (33)$$

When flow is absent ($\mathcal{R}=0$) things simplify considerably:

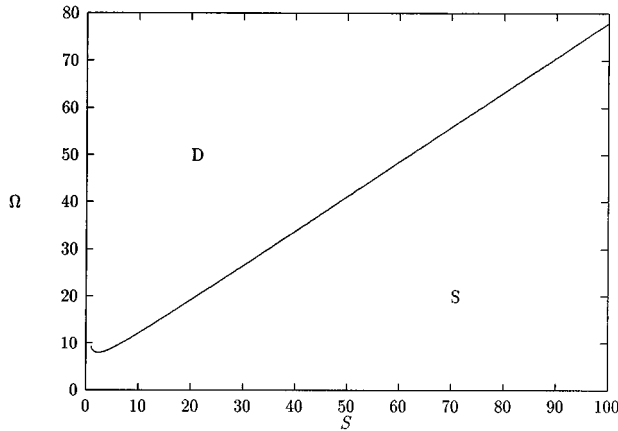$$\alpha_c^2 = \frac{k^2}{2(k+1)}, \qquad (34a)$$

Phys. Fluids, Vol. 8, No. 9, September 1996

T. P. Schulze and S. H. Davis   2325

FIG. 5. The curve $f_0 = 0$ in the Ω-S plane. If the frequency and Schmidt number are such that they lie below this curve, then the flow will have a stabilizing (S) influence on the interface for long-wave disturbances for all k and $\mathcal{R}$.

$$\mathcal{M}_c^{-1} = \frac{k^2}{4(k+1)}. \tag{34b}$$

If one takes the long-wave limit of the full linear-stability theory,[4] one recovers the result derived above after rescaling to the long-wave variables.

The flow term appearing in the characteristic equation is $\mathcal{R}^2 \alpha^3 f_0 / k$. Thus, we shall look at the sign of f_0 to determine whether the flow term has a stabilizing ($f_0 > 0$) or destabilizing ($f_0 < 0$) effect on the no-flow linear stability. Our previous work has shown that, in general, the influence of the flow is a complicated function of Schmidt number S, segregation coefficient k, surface energy parameter Γ, frequency Ω and amplitude R of the forcing.[4] A significant advantage of the long-wave limit is that f_0 depends only on S and Ω.

In Figure 5 we plot the curve $f_0 = 0$ in the S-Ω plane. Below this curve, the flow will have a stabilizing influence on long-wave disturbances for all k and $\mathcal{R}$. All combinations of S and Ω that lie on a given f_0 level curve give the same results, because these parameters do not enter into the analysis in any other way. Notice that the curve shown is almost linear for $S > 1$. Since the Schmidt number of most alloys lies between 10 and 1000, this curve is well approximated by its large-S asymptote for practical considerations:

$$\Omega \sim 0.73S + 4.7, \tag{35}$$

as $S \to \infty$.

The Schmidt number is a function of the materials being processed. The frequency, however, is a control parameter which can be adjusted, within practical limits, to achieve a stabilizing flow. One can optimize the stabilization by choosing Ω to maximize f_0. Surprisingly, the optimal condition for long-wave disturbances is to make the frequency as small as possible (the quasisteady limit). This contrasts with the results for the ASP which has a destabilizing influence on long-wave disturbances. Also, the results of the full linear stability analysis show that the stabilizing influence of the CSL in the quasisteady limit does not hold for $O(1)$ wave-

length disturbances (see Figure 3). Hence, it is unlikely that extremely small frequencies would prove effective in practice, and we shall choose for examples frequencies for which arbitrary wavelength disturbances are stabilized by the CSL according to the full linear stability analysis.[4]

According to the long-wave evolution equation, the magnitude of the stabilizing effect will increase monotonically with $\mathcal{R}$, provided $f_0 > 0$. If the other parameters are held fixed, the flow will eventually dominate and the interface will be stabilized. We see from equation (33), however, that the critical inverse morphological number can never be made equal to or less than zero; for the dominant term in equation (33) for small α is always positive. Thus, there is always some region near $\alpha = 0$ where $\mathcal{M}_c^{-1} > 0$. There is no finite value of $\mathcal{R}$ that can change this because the flow terms are proportional to α^3. This differs from the case where a finite amplitude velocity is imposed on the crystal interface.[5] In that case, the numerical results indicate that the neutral curve can be bounded below the horizontal axis ($M^{-1} = 0$) for a sufficiently strong flow. For the present case, one can certainly make the critical morphological number very large, and from a practical point of view that is all that matters.

When the system is near marginal stability, the exponential growth or decay indicated by the characteristic equation (30) is approximately correct for only a short time before nonlinear terms conspire to either dampen or accelerate this growth. To determine the weakly nonlinear evolution of a disturbance near marginal stability, we fix the wavenumber and morphological number at there critical values, and proceed to higher order in the small parameter δ. To this end, we identify $\mathcal{M}^{-1}$ as our bifurcation parameter, and expand it in a series for small δ:

$$\mathcal{M}^{-1} = \mathcal{M}_c^{-1} - \delta^2 \hat{m}/k + \dots . \tag{36}$$

The parameter m measures the degree of sub- or supercriticality.

For h_1 we write

$$h_1 = A(\mathcal{T})e^{i\alpha_c X} + \text{c.c.}, \tag{37}$$

where A is a slowly varying amplitude that evolves on a time scale, $\mathcal{T} = \delta^2 T$, even slower than the one previously identified for $T = \epsilon^4 t$.

In order for the equation at $O(\delta^3)$ to have periodic solutions, one must suppress secular terms which lead to unbounded growth. Equating the coefficients of such terms to zero gives the following Landau equation:

$$\alpha_c^2 (2 + 1/k) A_{\mathcal{T}} = \hat{m}A - \gamma_1 |A|^2 A, \tag{38}$$

where the Landau coefficient γ_1 is given by

$$\gamma_1 = -\left(\frac{3}{2} + 2P\right)\alpha_c^4, \tag{39}$$

and

$$P = \frac{-(4 + 2/k)\alpha_c^4}{15(1 + 1/k)\alpha_c^4 - 3k\alpha_c^2 + 7/4 \mathcal{R}^2 f_0 \alpha_c^3}. \tag{40}$$

In the absence of flow ($\mathcal{R} = 0$), it is known from the work of Wollkind and Segel[7] that long-wave, two-dimensional bifurcations are supercritical, and short-wave bi-
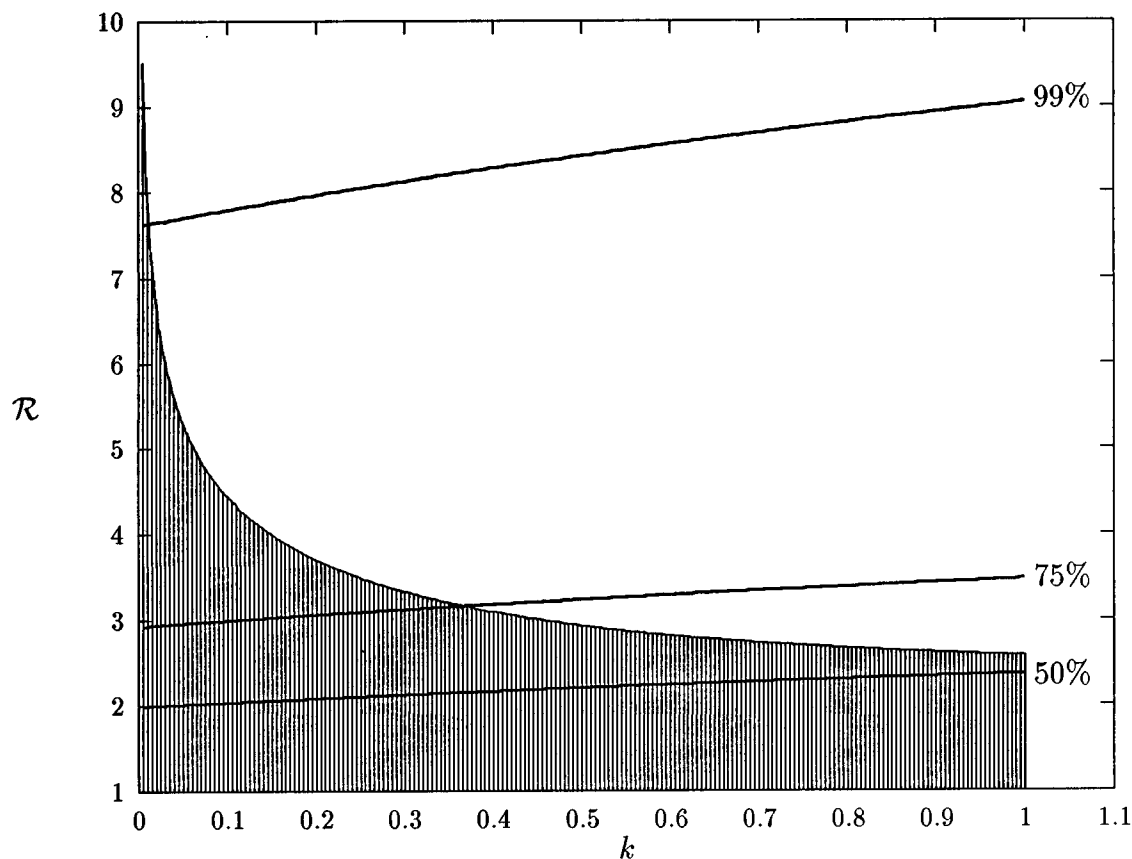
T. P. Schulze and S. H. Davis

FIG. 6. The three dark curves indicate values of $\mathscr{R}$ above which $\mathscr{M}_c^{-1}$ is reduced by a fixed percentage from its no-flow value, with the bottom, middle and top curves corresponding to a 50%, 75% and 99% reduction in the value of $\mathscr{M}_c^{-1}$, respectively. The curves are plotted as a function of k, which may range between zero and one for alloys that reject solute, and the remaining parameter values are $\Omega = 1$ and $S = 100$. The shaded region indicates a supercritical bifurcation and the unshaded region indicates a subcritical bifurcation.

furcations are subcritical. It turns out, however, that the addition of the flow can change the long-wave bifurcation from super- to subcritical as $\mathscr{R}$ is increased. These flow-induced subcritical bifurcations are a threat to our efforts to stabilize the interface because they lower the critical morphological number from the value indicated by linear theory. When $\mathscr{R}$ is just beyond this transition point, it is likely that there will be a turning point fairly close to the critical morphological number predicted by the linear theory, but as $\mathscr{R}$ increases further, it is conceivable that the system could be unstable to finite amplitude disturbances at morphological numbers for which the no-flow system is stable. We would like to determine the conditions for which the CSL method of stabilizing may prove useful, taking into account both the linear and weakly nonlinear theory. To this end, we wish to identify regions of the parameter space where the interface is linearly stable and the bifurcation is supercritical; for it is these regions that offer the best hope of producing a flat interface.

In Figure 6 the three dark curves indicate values of $\mathscr{R}$ above which $\mathscr{M}_c^{-1}$ is reduced by a fixed percentage from its no-flow value, with the bottom, middle and top curves corresponding to a 50%, 75% and 99% reduction in the value of $\mathscr{M}_c^{-1}$, respectively. The curves are plotted as a function of k, which may range between zero and one for alloys that reject solute, and the remaining parameter values are $\Omega = 1$

and $S = 100$. The shaded region indicates a supercritical bifurcation and the unshaded region indicates a subcritical bifurcation. When a dark curve passes through the shaded region, the shaded area above the curve indicates values of $\mathscr{R}$ for which the bifurcation is supercritical according to the weakly nonlinear theory and the flow has been stabilized by the indicated percentage according to linear theory. Examination of these figures reveals that a significant reduction in $\mathscr{M}_c^{-1}$ while maintaining a supercritical bifurcation can be accomplished provided the value of $\mathscr{R}$ is adjusted carefully.

There is very little qualitative change in this picture as one varies S and/or Ω, provided the value of f_0 remains positive (i.e., the parameter regime below the curve $f_0 = 0$ in Figure 5). Larger values of f_0, which changes more dramatically with the value of Ω than S, decrease the value of $\mathscr{R}$ at which the bifurcation switches from super- to subcritical. Similarly, smaller values of f_0 increase this value. The same trend is followed by the curves indicating a fixed percentage of stabilization, and the relative position of the curves shown in Figure 6 does not change much for different values of $f_0 > 0$. For example, see Figure 7, which is analogous to Figure 6 with a value of $\Omega = 10$ instead of $\Omega = 1$. As the value of f_0 approaches zero from above, the curves in these figures continue to rise, and disappear entirely for $f_0 \lesssim 0$. When $f_0 \lesssim 0$ the flow destabilizes the interface and bifurca-
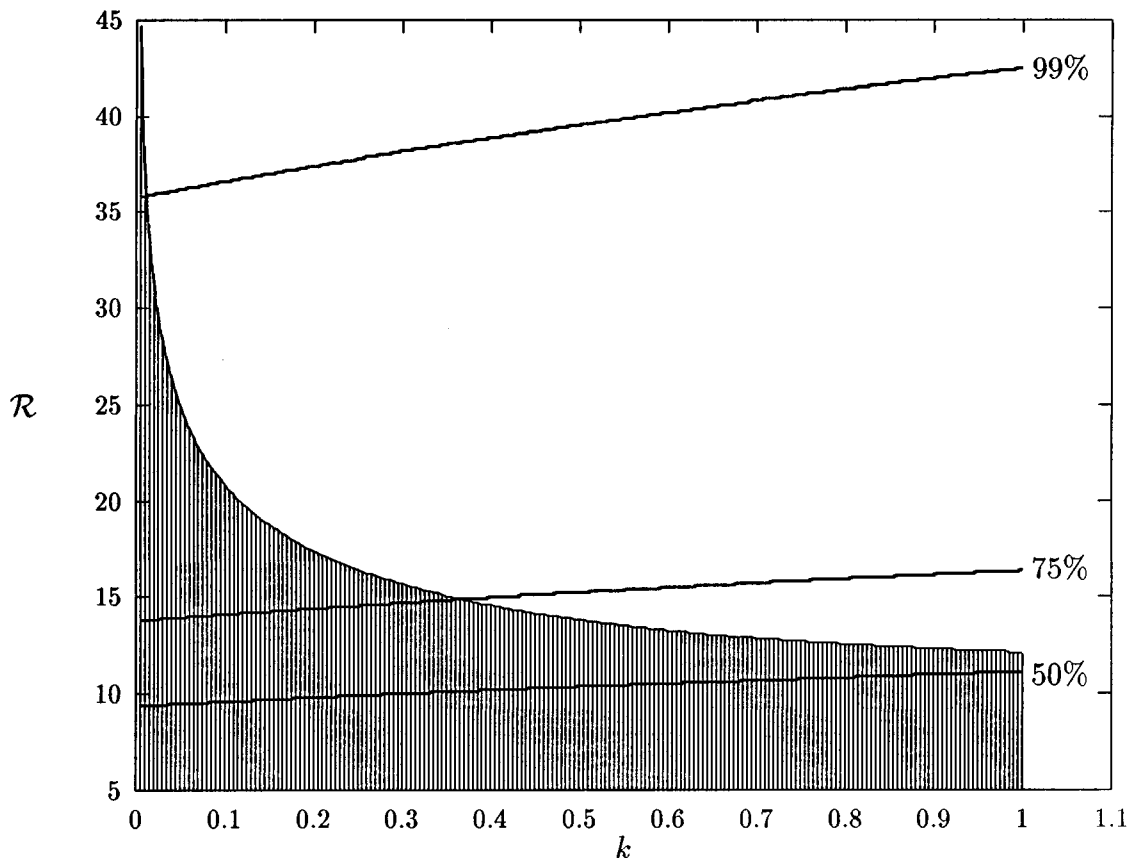
FIG. 7. The three dark curves indicate values of $\mathscr{R}$ above which $\mathscr{M}_c^{-1}$ is reduced by a fixed percentage from its no-flow value, with the bottom, middle and top curves corresponding to a 50%, 75% and 99% reduction in the value of $\mathscr{M}_c^{-1}$, respectively. The shaded region indicates a supercritical bifurcation and the unshaded region indicates a subcritical bifurcation. The curves are plotted as a function of k, which may range between zero and one for alloys that reject solute, and the remaining parameter values are $\Omega = 10$ and $S = 100$. Notice that this figure is essentially the same as the previous one except for a change in the scale of $\mathscr{R}$.

tions are always supercritical. The magnitude of destabilization is very small, however, and very large values of $\mathscr{R}$ would be necessary to produce a significant effect.

V. THREE-DIMENSIONAL PATTERN SELECTION

While results in two dimensions may apply to experiments in which the alloy is placed in a Hele-Shaw cell, the majority of applications must be considered as three-dimensional. In three dimensions we consider the influence of two perpendicular crystal oscillations, producing a three-dimensional version of the CSL. When the phase difference γ between the two oscillations is an integral multiple of π, we have the special case of a planar oscillation, and the results are the same as for the two-dimensional case discussed in the previous section. This type of flow does not stabilize the three-dimensional system. When destabilizing, two-dimensional cells will form of the flow and the bifurcations will be governed by the amplitude equation derived in the previous section. We shall refer to this pattern as ''rolls'' in analogy to the more familiar pattern observed in convection experiments. When stabilizing, cells will form in the direction parallel to the flow, the critical morphological number will be unchanged and bifurcations will be governed by

the same amplitude equation minus the flow terms. In this case, the linear theory predicts that the only effect of the flow is to choose cell orientation.

For $\gamma \neq n\pi$, the motion of the crystal is in elliptical orbits, and according to the linear theory, it is possible for a sufficiently strong flow to eliminate the instability for a large range of parameter values.[5] When the motion of the crystal is in a noncircular ellipse, the symmetry of the system is broken, and two-dimensional cells are again the preferred pattern at onset. When the instability persists, but the flow is stabilizing (i.e., the flow increases the critical morphological number), the cells will orient themselves along the minor axis of the ellipse, which is the direction least stabilized by the flow. When the flow is destabilizing, the cells will orient themselves along the major axis of the ellipse.

We examine the linear stability of a single oblique roll solution by assuming normal modes of the form

$$h(X,Y) = A e^{i\mathbf{a}\cdot\mathbf{X}} + \text{c.c.}, \tag{41}$$

in equation (23). Here we have once again omitted the subscript zero on h, and we have already set the growth rate and wave speed to zero, so that we are seeking neutrally stable, stationary solutions which have the physical form of an infinite sheet of parallel cells with a wavevector $|\mathbf{a}|$ ori-

ented at an angle $\theta = \tan^{-1}(\alpha_2/\alpha_1)$ with respect to the X-axis and a wavenumber $\alpha \equiv |\mathbf{a}| = \sqrt{\alpha_1^2 + \alpha_2^2}$.

The neutral stability surface is now given by

$$
\begin{aligned}
k\mathcal{M}^{-1} &= k\alpha^2 - (1+1/k)\alpha^4 - \mathcal{R}^2 f_0 \alpha |\mathbf{r}\cdot\mathbf{a}|^2 \\
&= k\alpha^2 - \left(1 + \frac{1}{k}\right)\alpha^4 - \frac{1}{4}\mathcal{R}^2 f_0 \alpha^3 [(\cos\theta \\
&\quad + \beta\cos\gamma\sin\theta)^2 + \beta^2\sin^2\theta\sin^2\gamma].
\end{aligned}
\tag{42}
$$

The dependence on the phase difference between the two oscillation γ and the amplitude ratio β is analogous to that found by Kelly and Hu[6] in their study of the influence of nonplanar oscillations on Bénard convection. From equation (42) we see that the critical morphological number is a function of the disturbance orientation. As a result, the flow will select a preferred orientation for developing cells, as described above.

When considering the weakly nonlinear analysis in the elliptical case, we shall look only at the most unstable cell orientation. The weakly nonlinear development of these cells will be governed by the same amplitude equation found in the two-dimensional case with the flow amplitude $\mathcal{R}$ replaced by $\mathcal{R}' = \mathcal{R}[(\cos\theta_c + \beta\cos\gamma\sin\theta_c)^2 + \beta^2\sin^2\theta_c\sin^2\gamma]^{1/2}$, where θ_c is the angle that the wavevector of the critical disturbance makes with the X-axis. With this new interpretation of $\mathcal{R}$ the results in the figures of Section IV still apply.

As it turns out, elliptical oscillations may provide the best hope for suppressing morphological instability in three dimensions because of their symmetry breaking feature. In the case of circular oscillations, the critical morphological number is the same for cells oriented in every direction. This lack of a preferred orientation makes it possible for a superposition of cells with the same wavenumber to grow at onset. Some of these superposition patterns bifurcate transcritically, and therefore always pose the threat of a subcritical instability that will reduce the stabilization indicated by the linear theory. These more complicated three-dimensional patterns are likely to emerge in the case of elliptical oscillations as well, but only as secondary bifurcations for larger amplitude disturbances or for small amplitude disturbances when the motion of the crystal is nearly circular.

When the amplitudes of the two oscillations are the same and the phase difference is $\pi/2$ we have the special case of circular orbits. In this case, as in the no-flow case, there is no preferred direction for cells to orient themselves, and more complicated patterns are possible at onset. Because these are both laterally isotropic cases, squares and hexagons are the likely patterns. When the crystal motion is in a circular pattern, we shall be interested in both when instability occurs and what type of pattern emerges as a result.

A. Squares

Square patterns are the result of the simultaneous growth of two perpendicular roll patterns. In order to consider the instability of two perpendicular cellular solutions near onset,

we must restore the symmetry of the linear operator by considering circular orbits of the crystal. To this end, we set $\beta = 1$ and $\gamma = \pi/2$ in equation (6).

We then derive the amplitude equations by assuming a leading-order solution of the form

$$
h_1 = A(\mathcal{T})e^{i\alpha X} + B(\mathcal{T})e^{i\alpha Y} + \text{c.c.}
\tag{43}
$$

This solution will satisfy the linearized evolution equation provided the morphological number lies on the neutral curve identified by equation (33). Note that, due to the circular symmetry, the orientation of the square lattices can be fixed without loss of generality.

Secular terms again appear at $O(\delta^3)$ and their elimination leads to two coupled Landau equations:

$$
\alpha_c^2(2+1/k)A_{\mathcal{T}} = \hat{m}A - (\gamma_1|A|^2 + \gamma_2|B|^2)A,
\tag{44a}
$$

$$
\alpha_c^2(2+1/k)B_{\mathcal{T}} = \hat{m}B - (\gamma_2|A|^2 + \gamma_1|B|^2)B,
\tag{44b}
$$

where

$$
\gamma_1 = -\alpha^4[3/2 + 2(2+1/k)P_1],
\tag{45a}
$$

$$
\gamma_2 = -\alpha^4[1 + 2(2-1/k)P_2],
\tag{45b}
$$

and

$$
P_1 = \frac{-2\alpha^4(2+1/k)}{15(1+1/k)\alpha^4 - 3k\alpha^2 + \frac{7}{4}\mathcal{R}^2 f_0 \alpha^3},
\tag{46a}
$$

$$
P_2 = \frac{-2\alpha^4}{k[3(1+1/k)\alpha^4 - k\alpha^2 + (2\sqrt{2}-1)/4]\mathcal{R}^2 f_0 \alpha^3]}.
\tag{46b}
$$

Equations (44) have four types of stationary solutions:

$$
|A| = |B| = 0,
\tag{47a}
$$

$$
|A| = \sqrt{\hat{m}/\gamma_1} > 0; |B| = 0,
\tag{47b}
$$

$$
|A| = 0; |B| = \sqrt{\hat{m}/\gamma_1} > 0,
\tag{47c}
$$

$$
|A| = |B| = \sqrt{\hat{m}/(\gamma_1 + \gamma_2)} > 0.
\tag{47d}
$$

The first of these solutions corresponds to the basic state. The second and third solutions correspond to two-dimensional cells aligned with the X- and Y-axis, respectively. These solutions bifurcate supercritically for $\gamma_1 > 0$ and subcritically for $\gamma_1 < 0$. The third solution corresponds to a square pattern aligned with the axes. This solution bifurcates supercritically for $\gamma_1 + \gamma_2 > 0$ and subcritically for $\gamma_1 + \gamma_2 < 0$. These results, along with the eigenvalues for the linearized system are summarized in Table I. Using these results, one may predict when stable squares or two-dimensional cells are the preferred pattern.

In Figure 8 we interpret these results in terms of the parameters in the governing equations. The plot is once again in the k-$\mathcal{R}$ plane, and the curve indicating transition from super- to subcritical instability for rolls is the same as shown in Figures 6 and 7. The other solid curve in this picture separates the regions where square solutions bifurcate sub- or supercritically. When bifurcations are subcritical ($\hat{m} < 0$), none of the bifurcating solutions are stable. However, when $\hat{m} > 0$ the supercritical region of the figure can be subdivided. Stable two-dimensional cells are the preferred

TABLE I. The steady solutions of the two-mode amplitude equations, the eigenvalues of the linearized system and the range of coefficients for which the solution exists and is stable.

Cell type	Solution	Eigenvalues	Stable solution range
None	$|A|=|B|=0$	$\hat{m},\hat{m},\hat{m}$	$\hat{m}<0$
2D	$|A|=\sqrt{\hat{m}/\gamma_1}>0,|B|=0$ $|B|=\sqrt{\hat{m}/\gamma_1}>0,|A|=0$	$-2\hat{m},\hat{m}(1-\gamma_2/\gamma_1)$	$\hat{m}>0,\gamma_2>\gamma_1>0$
Square	$|A|=|B|=\sqrt{\hat{m}/(\gamma_1+\gamma_2)}$	$-2\hat{m},$ $-2\hat{m}(\gamma_1-\gamma_2)/(\gamma_1+\gamma_2)$	$\hat{m}>0,\gamma_1>|\gamma_2|$

pattern for a range of segregation coefficients. Just outside this range there is a region where stable squares are the preferred pattern. The other regions correspond to unstable solutions, some of which may be supercritical bifurcations. Increasing the flow amplitude reduces the range of segregation coefficients corresponding to stable square solutions. If the flow-amplitude is increased sufficiently, all bifurcations become subcritical. For extreme values of the segregation coefficient squares always bifurcate subcritically and are unstable; thus it is impossible to identify regions with significant flow-stabilization and supercritical bifurcations. Unstable supercritical squares, which are impossible without flow, exist in the region bounded by the two solid curves.

As with the two-dimensional results, the scale of the $\mathcal{R}$-axis in Figure 8 is augmented by adjusting the value of S or Ω. Changes in these parameter values that increase the magnitude of f_0 increase the influence of the flow and lower the curves in the figure. Changes that decrease f_0 decrease the influence of the flow and raise the curves. Once again, there are no qualitative changes until f_0 is reduced below zero, at which point the flow becomes very weak, slightly destabilizing and the no-flow bifurcation structure is essentially unaltered.

These equations cannot tell us if the system eventually saturates at some superposition state other than rolls or squares. Furthermore, we cannot say how these other states would compete with the squares even when the squares exist and are linearly stable according to equations (44). In fact, based on experimental evidence,[21] it is known that hexagonal solutions are a likely alternative to square solutions, and we shall discuss this possibility next.
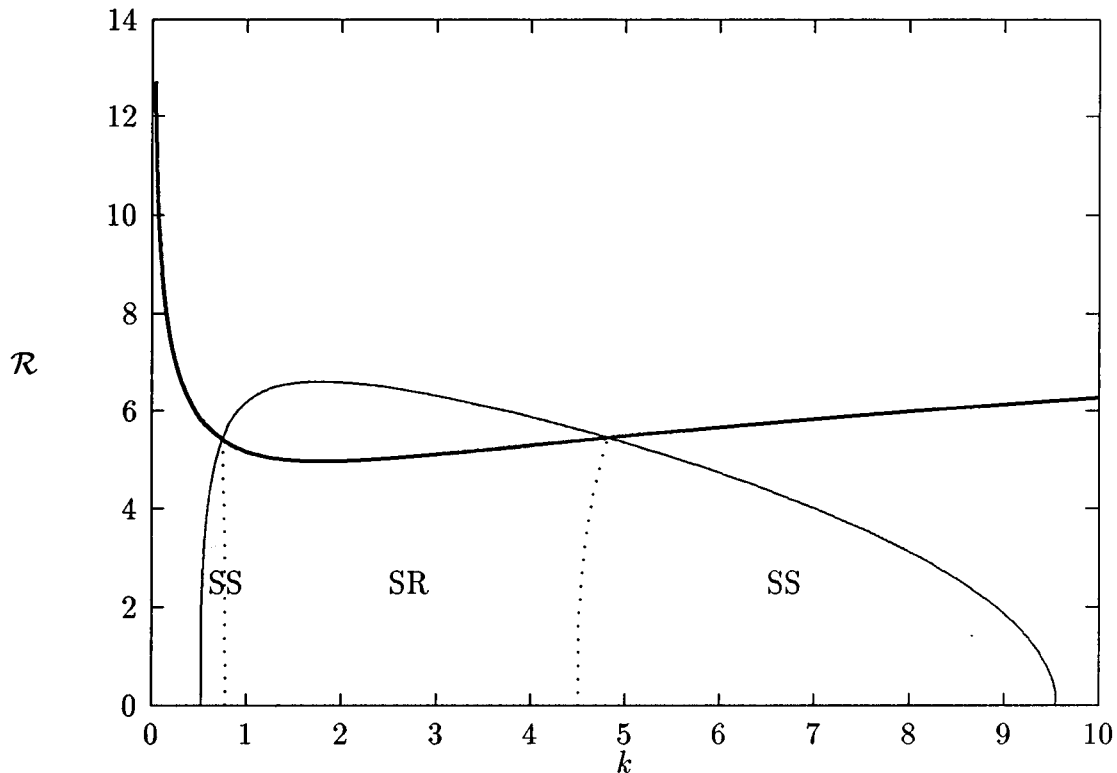

FIG. 8. A map in the k-$\mathcal{R}$ plane showing regions where rolls (SR) or squares (SS) are the preferred stable state. The unmarked regions correspond to unstable solutions. Rolls bifurcate subcritically (supercritically) above (below) the darker solid curve which spans all values of k. Squares bifurcate subcritically (supercritically) above (below) the lighter solid curve which spans a limited range of segregation coefficients. The other parameter values are $S=100$ and $\Omega=1$. Recall that solute is preferentially incorporated into the solid for $k>1$.

B. Hexagons

For the case of hexagonal cells, consider the superposition of three two-dimensional cell patterns oriented at $2\pi/3$ rad with respect to one another. The leading-order solution is then of the form

$$h_1 = A(\mathscr{T})e^{i\alpha\mathbf{n}_1\cdot\mathbf{X}} + B(\mathscr{T})e^{i\alpha\mathbf{n}_2\cdot\mathbf{X}} + C(\mathscr{T})e^{i\alpha\mathbf{n}_3\cdot\mathbf{X}} + \text{c.c.},$$
(48)

where the $\mathbf{n}_i$ are normal vectors in the X-Y plane separated by $2\pi/3$ rad. The orientation of the three vectors with respect to the axis is arbitrary, with all orientations leading to the same amplitude equations.

At $O(\delta^2)$ we have

$$\mathscr{L}h_2 = -\nabla^2|\nabla h_1|^2 - \frac{1}{k}\nabla\cdot(\nabla^2 h_1\nabla h_1)$$

$$= -2(2+1/k)\alpha^4[A^2e^{2i\alpha\mathbf{n}_1\cdot\mathbf{X}} + B^2e^{2i\alpha\mathbf{n}_2\cdot\mathbf{X}}$$

$$+ C^2e^{2i\alpha\mathbf{n}_3\cdot\mathbf{X}}]$$

$$- 3(1+1/k)\alpha^4[AB^*e^{i\alpha(\mathbf{n}_1-\mathbf{n}_2)\cdot\mathbf{X}} + AC^*e^{i\alpha(\mathbf{n}_1-\mathbf{n}_3)\cdot\mathbf{X}}$$

$$+ BC^*e^{i\alpha(\mathbf{n}_2-\mathbf{n}_3)\cdot\mathbf{X}}]$$

$$\times (1-1/k)\alpha^4[ABe^{i\alpha(\mathbf{n}_1+\mathbf{n}_2)\cdot\mathbf{X}}$$

$$+ ACe^{i\alpha(\mathbf{n}_1+\mathbf{n}_3)\cdot\mathbf{X}} + BCe^{i\alpha(\mathbf{n}_2+\mathbf{n}_3)\cdot\mathbf{X}} + \text{c.c.}],$$
(49)

where $\mathscr{L}$ is the same linear operator found in equation (23) with $\mathscr{M}$ replaced by $\mathscr{M}$-critical and $|\mathbf{r}\cdot\nabla|^2 = \frac{1}{4}\nabla^2$.

Some of the terms appearing on the right-hand side of this equation have wavevectors whose moduli are unity, making them secular. If one suppresses these terms in the usual way, time must be scaled on δ rather than δ^2. The resulting evolution equation will only have quadratic nonlinearities, and all bifurcations will be to transcritical hexagons. This means that the potential for subcritical instabilities always exists for this flow configuration, and will negate at least some of the stabilization predicted by the linear theory. The extent to which this is true depends on the location of the turning point for the bifurcating solution which, in general, may not be determined by a weakly nonlinear analysis. When the coefficients of the secular terms are $O(\delta)$, however, the need to suppress these terms is delayed to higher order, where the resulting amplitude equation will have cubic as well as quadratic nonlinearities. When this is the case, the location of the turning point may be determined by a weakly nonlinear analysis. In the present problem, the terms in question may be made small by assuming that the segregation coefficient k lies within $O(\delta)$ of unity.

In order to proceed to higher order we shall then assume

$$k \sim 1 + \mathscr{K}\delta + \dots,$$
(50)

for $\mathscr{K}\sim O(1)$.

At $O(\delta^3)$ suppressing secular terms leads to three coupled amplitude equations of the form

$$3\alpha^2 A_{\mathscr{T}} = \hat{m}A + \gamma_0 B^*C^* - (\gamma_1|A|^2 + \gamma_2|B|^2 + \gamma_2|C|^2)A,$$
(51a)

$$3\alpha^2 B_{\mathscr{T}} = \hat{m}B + \gamma_0 A^*C^* - (\gamma_2|A|^2 + \gamma_1|B|^2 + \gamma_2|C|^2)B,$$
(51b)

$$3\alpha^2 C_{\mathscr{T}} = \hat{m}C + \gamma_0 B^*A^* - (\gamma_2|A|^2 + \gamma_2|B|^2 + \gamma_1|C|^2)C,$$
(51c)

where

$$\gamma_0 = \mathscr{K}\alpha^4,$$
(52a)

$$\gamma_1 = -\alpha^4(3/2 + 6P_1),$$
(52b)

$$\gamma_2 = -\alpha^4(3/2 + 3P_2),$$
(52c)

and

$$P_1 = \frac{-6\alpha^4}{30\alpha^4 - 3\alpha^2 + (7/4)\mathscr{R}^2 f_0\alpha^3},$$
(53a)

$$P_2 = \frac{-6\alpha^4}{16\alpha^4 - 2\alpha^2 - [(1-3\sqrt{3})/4]\mathscr{R}^2 f_0\alpha^3}.$$
(53b)

Notice that P_1 is the same as for the case of a square pattern if $k \sim 1$. This is not the case for P_2, however.

In the case of rolls and squares, only the moduli of the cell amplitudes are important for classifying solutions. This is because a change in the sign of the amplitude results in another solution which is distinguishable only by a translation in the X-Y plane. Changing the sign of a solution to equations (51) will still result in a solution; however, the new solution may or may not be physically distinguishable from the original.

In general, the amplitudes determined by equations (51) are complex. To determine the steady solutions and analyze their behavior, it is convenient to represent each of the amplitudes in complex-polar notation:

$$A = \rho_A e^{i\phi_A}, \quad B = \rho_B e^{i\phi_B}, \quad C = \rho_C e^{i\phi_C},$$
(54)

and separate the amplitude equations into real and imaginary parts:

$$m\rho_A + \gamma_0\rho_B\rho_C\cos(\phi_A + \phi_B + \phi_C) - (\gamma_1\rho_A^2 + \gamma_2\rho_B^2 + \gamma_2\rho_C^2)\rho_A = 0,$$
(55a)

$$m\rho_B + \gamma_0\rho_A\rho_C\cos(\phi_A + \phi_B + \phi_C) - (\gamma_1\rho_A^2 + \gamma_2\rho_B^2 + \gamma_2\rho_C^2)\rho_B = 0,$$
(55b)

$$m\rho_C + \gamma_0\rho_B\rho_A\cos(\phi_A + \phi_B + \phi_C) - (\gamma_1\rho_A^2 + \gamma_2\rho_B^2 + \gamma_2\rho_C^2)\rho_C = 0,$$
(55c)

$$\sin(\phi_A + \phi_B + \phi_C) = 0.$$
(55d)

These equations are underdetermined due to translational symmetry in the X-Y plane. Thus the fourth equation may be satisfied by any total $\phi_A + \phi_B + \phi_C$ equal to an integral multiple of π. The even and odd multiples of π separate the remaining equations into two cases which differ in the sign of the quadratic terms. It is convenient for illustrative purposes to choose two of the phase angles, say ϕ_B and ϕ_C, to be zero. The third phase angle will then be an integral multiple of π and all of the amplitudes will be real.

A bifurcation diagram, such as the one shown in Figure 9, is a convenient way to sort out the possible solutions to these equations. This figure is for no flow, and is valid for k sufficiently close to unity. As the flow amplitude is in-

Phys. Fluids, Vol. 8, No. 9, September 1996
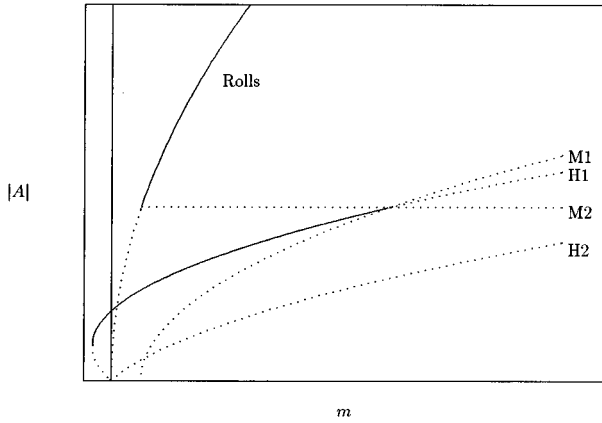
T. P. Schulze and S. H. Davis   2331

FIG. 9. Bifurcation diagram for the system when $\mathscr{R}=0$. Stable solutions (unstable) are indicated with solid (dotted) curves. The curves marked "H1" and "H2" correspond to hexagonal nodes and cells respectively. The curves marked "M1" and "M2" correspond to two distinct mixed-mode solutions. The diagram is presented without scales because its qualitative features are representative for a wide range of $\mathscr{R}$ values.

creased the structure of this diagram is compressed into a narrower range of $\hat{m}$ values, but remains qualitatively similar until $\mathscr{R}$ exceeds a critical value. The diagram is symmetric with respect to the A-axis, and only the upper portion is shown. The diagrams for the amplitudes B and C versus m are identical to that for A.

When two of the three amplitudes are zero, two-dimensional cells are once again solutions with, say, $\rho_A^2 = \hat{m}/\gamma_1$. These solutions are unstable when they bifurcate subcritically (which does not occur when there is no flow). These solutions are initially unstable when they bifurcate supercritically, but become stable when they intersect a secondary bifurcation at $\hat{m} = \gamma_1 \gamma_0^2/(\gamma_1 - \gamma_2)^2$.

When all three of the amplitudes are equal, the solutions are hexagonal with either

$$\rho_A = \rho_B = \rho_C = \frac{\gamma_0 \pm \sqrt{\gamma_0^2 + 4\hat{m}(\gamma_1 + 2\gamma_2)}}{2(\gamma_1 + 2\gamma_2)} \qquad (56)$$

or

$$\rho_A = \rho_B = \rho_C = \frac{-\gamma_0 \pm \sqrt{\gamma_0^2 + 4\hat{m}(\gamma_1 + 2\gamma_2)}}{2(\gamma_1 + 2\gamma_2)}, \qquad (57)$$

depending on the sign of the quadratic terms. These bifurcations are transcritical and take the form of parabolas in the bifurcation diagram. There are turning points located at $\hat{m} = -\gamma_0^2/2(\gamma_1 + 2\gamma_2)$, $\rho = \pm \gamma_0/2(\gamma_1 + 2\gamma_2)$. For a sufficiently weak flow, these parabolas open to the right and the branches with the larger magnitude amplitudes are initially unstable, switching to stable at the turning points. These branches are then stable from the turning point until they intersect secondary bifurcations at $\hat{m} = \gamma_0^2(2\gamma_1 + \gamma_2)/(\gamma_1 - \gamma_2)^2$. The branches with the smaller magnitude amplitudes are unstable.

The two types of hexagonal solutions differ only in sign. However, because the solutions are not symmetric about the $\zeta = 0$ plane, the two solutions result in different patterns of solute distribution in the solid. In one case, the local maxima

are more pronounced than the local minima, while in the other case, the local minimums are more pronounced. Note that, for $k < 1$, the solute distribution will be out of phase with the interface height, as the solute concentration is lower away from the interface. When $k < 1$ the upper hexagonal branch in Figure 9 corresponds to hexagonal nodes, and the lower branch to hexagonal cells.

Finally, when two of the amplitudes are equal but nonzero, we have what are called "class V," or mixed mode solutions:

$$\rho_A = \frac{-\gamma_0}{\gamma_1 - \gamma_2}, \qquad (58a)$$

$$\rho_B = \rho_C = \sqrt{\frac{\hat{m}(\gamma_1 - \gamma_2)^2 - \gamma_1 \gamma_0^2}{(\gamma_1 + \gamma_2)(\gamma_1 - \gamma_2)^2}}. \qquad (58b)$$

The amplitudes may be permuted to give still other solutions, which are identical in form. In total there are six different solutions if one accounts for these permutations and the possible sign change of the quadratic terms. Note that the two mixed-mode branches in the diagram actually correspond to different solutions. The eigenvalues for the mixed mode were not calculated; however, their stability would be inconsistent with the structure of the bifurcation diagram, so we shall assume they are unstable.

There are no solutions with all of the ρ distinct from one another.

As $\mathscr{R}$ is increased for a stabilizing flow, the bifurcation diagram shown in Figure 9 is compressed in the horizontal direction; the bifurcation structure remains unchanged until a critical value of $\mathscr{R}$ is reached. This structure features two hysteresis loops: one is due to the very shallow turning point of the hexagonal solutions, and the other occurs because of the changes in stability when the mixed mode solutions are intersected by the roll and hexagon solutions. Beyond this critical value of $\mathscr{R}$, the roll solutions become subcritical. This is the same transition which occurs for the two-dimensional cells, and is determined by the value of $\mathscr{R}$ which makes $\gamma_1 = 0$. At a second value of $\mathscr{R}$, which tends to be numerically close to this first transition, there is a singularity that causes the turning point of the hexagonal solutions to approach negative infinity. The location of the second transition point is determined by the value of $\mathscr{R}$ which makes $\gamma_1 = -2\gamma_2$. Beyond the immediate vicinity of this second critical value of $\mathscr{R}$, which is in the neighborhood of $\mathscr{R} = 6$ when $S = 100$ and $\Omega = 1$, the parabolas in the bifurcation diagram flip so that they open to the left. The mixed-mode solutions make a similar transition, so that the entire bifurcation diagram essentially reflects over the vertical axis as $\mathscr{R}$ is increased. An example of a bifurcation diagram when the value of $\mathscr{R}$ is beyond these transition points is shown in Figure 10. All of the solutions are unstable. One structural distinction from the small $\mathscr{R}$ case is that the lower, rather than the upper, hexagonal branch is now the one that intersects the mixed-mode branch. The new intersection point is give by $\hat{m} = 3\gamma_0^2 \gamma_2/(\gamma_1 - \gamma_2)^2$.

As $\mathscr{R}$ is increased, the transition of the bifurcations can be viewed as a change from super- to subcritical solutions, as the turning point of the hexagonal branch is very close to the
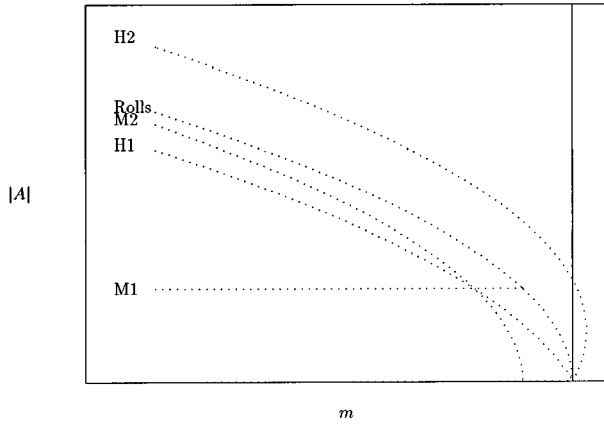
FIG. 10. Bifurcation diagram for the system when $\mathscr{R}=5.7$, $\Omega=1$ and $S=100$. Stable solutions (unstable) are indicated with solid (dotted) curves. Note that the only stable solution is the flat interface up to the critical point. The curves marked ''H1'' and ''H2'' correspond to hexagonal nodes and cells, respectively. The curves marked ''M1'' and ''M2'' correspond to two distinct mixed-mode solutions. The diagram is presented without scales because its qualitative features are representative for a wide range of $\mathscr{R}$ values.

VI. CONCLUSION

In this paper, we derived a strongly nonlinear evolution equation for the shape of a directionally solidifying interface in the presence of a three-dimensional compressed Stokes layer. We used a one-sided model, where diffusion of solute in the solid is neglected, and we invoked the frozen temperature approximation.[20] The equation is valid when (1) the surface energy parameter Γ is near the absolute stability boundary $\Gamma_s=1/k$; (2) the imposed flow is weak; and (3) equilibrium thermodynamics hold. Under these conditions, the critical disturbance wavelength is long compared to the diffusion length scale D/V and the critical morphological number is large. We then presented the results of a weakly nonlinear analysis of the evolution equation in two and three dimensions.

In previous work we had determined that increasing the flow amplitude $\mathscr{R}$ could stabilize the interface, provided the frequency of the flow oscillations is within a calculated range. The stabilization was particularly effective in the long-wave regime. The two-dimensional bifurcation analysis showed that increasing the amplitude of the CSL will eventually change bifurcations from super- to subcritical when the flow is in the stabilizing parameter regime. Thus, at least some of the stabilization gained according to the linear theory is lost to subcritical instabilities if the flow amplitude is made too large; yet it is still possible to stabilize within a range of $\mathscr{R}$ values for which the bifurcation is supercritical and, presumably, one could increase $\mathscr{R}$ at least somewhat beyond this range before the subcritical instability would ne-

origin compared to the other structure in the diagram. Thus, in general, increasing the flow amplitude seems to favor subcritical solutions for rolls, squares and hexagons.

These results are summarized in Table II. We have not calculated the eigenvalues for the mixed modes as they are complicated solutions to a nontrivial cubic polynomial.

TABLE II. The steady solutions of the three-mode amplitude equations and the eigenvalues of the linearized system. The table is for $\mathscr{K}>1$. For $\mathscr{K}<1$ the hexagonal nodes and cells are reversed.

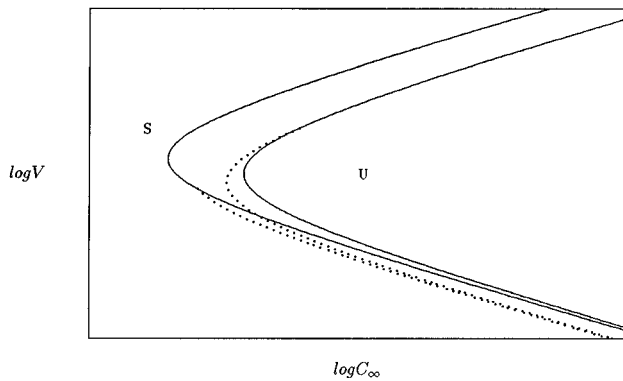| Description	Solutions	Eigenvalues
Planar	$\rho_A=\rho_B=\rho_C=0$	$\hat{m},\hat{m},\hat{m}$
2D cells	$\rho_A=\sqrt{\hat{m}/\gamma_1},\rho_B=\rho_C=0$ $\rho_B=\sqrt{\hat{m}/\gamma_1},\rho_A=\rho_C=0$ $\rho_C=\sqrt{\hat{m}/\gamma_1},\rho_A=\rho_B=0$	$-2\hat{m},$ $\hat{m}(1-\gamma_2/\gamma_1)\pm\gamma_0\sqrt{\hat{m}/\gamma_1}$
Hexagonal nodes	$\rho_A=\rho_B=\rho_C=\pm\dfrac{\gamma_0+\sqrt{\gamma_0^2+4\hat{m}(\gamma_1+2\gamma_2)}}{2(\gamma_1+2\gamma_2)}$	$\hat{m}\mp\gamma_0\rho_A-3\rho_A^2\gamma_1-\rho_A^2\gamma_2,$ $\hat{m}\mp\gamma_0\rho_A-3\rho_A^2\gamma_1-\rho_A^2\gamma_2,$ $\hat{m}\pm2\gamma_0\rho_A-3\rho_A^2\gamma_1-4\rho_A^2\gamma_2$
Hexagonal cells	$\rho_A=\rho_B=\rho_C=\pm\dfrac{\gamma_0-\sqrt{\gamma_0^2+4\hat{m}(\gamma_1+2\gamma_2)}}{2(\gamma_1+2\gamma_2)}$	$\hat{m}\pm\gamma_0\rho_A-3\rho_A^2\gamma_1-\rho_A^2\gamma_2,$ $\hat{m}\pm\gamma_0\rho_A-3\rho_A^2\gamma_1-\rho_A^2\gamma_2,$ $\hat{m}\mp2\gamma_0\rho_A-3\rho_A^2\gamma_1-4\rho_A^2\gamma_2$
Mixed modes	$\rho_A=\pm\gamma_0/(\gamma_1-\gamma_2),$ $\rho_B=\rho_C=\sqrt{\dfrac{\hat{m}(\gamma_1-\gamma_2)^2-\gamma_1\gamma_0^2}{(\gamma_1-\gamma_2)^2(\gamma_1+\gamma_2)}}$ $\rho_B=\pm\gamma_0/(\gamma_1-\gamma_2),$ $\rho_A=\rho_C=\sqrt{\dfrac{\hat{m}(\gamma_1-\gamma_2)^2-\gamma_1\gamma_0^2}{(\gamma_1-\gamma_2)^2(\gamma_1+\gamma_2)}}$ $\rho_C=\pm\gamma_0/(\gamma_1-\gamma_2),$ $\rho_B=\rho_A=\sqrt{\dfrac{\hat{m}(\gamma_1-\gamma_2)^2-\gamma_1\gamma_0^2}{(\gamma_1-\gamma_2)^2(\gamma_1+\gamma_2)}}$	see the text

FIG. 11. Conjectured stability diagram for the strongly stabilized system. The curves are given in dimensional form—V versus C_∞ with a fixed temperature gradient G. The (solid) neutral curves are based on linear theory for the no-flow[2] (outer) and strongly stabilized[5] (inner) cases. The dashed curves extending from the neutral curves are assumed to give a qualitative description of the manner in which subcritical instabilities lower the critical value of the concentration. For a given case, the interface is assumed stable (S) when the far-field concentration is to the left of both the solid and dashed curves.

gate the stabilization indicated by the linear theory.

In light of the nonlinear results presented here, it appears that effective stabilization of the two-dimensional system using the CSL will require careful control of both the amplitude and frequency of the flow. In Figure 11 we present a conjectured version of the stability diagram when the system is optimally stabilized by a CSL. The linear-theory neutral curves are known exactly, but we have assumed, based on our long-wave results, that a strongly stabilizing flow will move the transition from sub- to supercritical bifurcations around the nose of the curve and toward the absolute stability limit. In the subcritical regions, we have assumed that the critical value of the concentration is lowered, but by a limited amount—due either to the presence of a turning point in the bifurcation diagram or to the finite amplitude of noise in the system. In particular, we assume that the subcritical instability will become negligible as one approaches the transition point.

For the three-dimensional system we examined bifurcations to steady roll, square and hexagonal solutions. When the motion of the crystal is in a noncircular elliptical pattern, rolls are the only primary bifurcation in the weakly nonlinear limit though others may occur as secondary states.

When the motion of the crystal is in a circular pattern, the system is isotropic in the plane of the interface, and superposition states involving more than one set of obliquely positioned rolls are possible. This flow may be useful for selecting a preferred pattern among these states, allowing a crystal grower more control over crystal microstructure.

We examined the competition between roll and square solutions, and found that increasing the flow amplitude tends to reduce, and eventually eliminate, the range of segregation coefficients for which stable square solutions are possible. Increasing the flow amplitude favors subcritical instabilities for both squares and rolls. Unlike the no-flow case, unstable,

supercritically bifurcating square solutions are possible for a small range of $\mathscr{R}$ values.

Next we examined the competition between roll and hexagonal solutions. For values of k away from unity, unstable hexagons bifurcate transcritically and are the only bifurcating solution in the weakly nonlinear limit. When k is sufficiently close to unity, the cubic and quadratic nonlinearities in the evolution equation are balanced, and a complicated bifurcation structure emerges. As with the square and roll solutions, bifurcations to rolls are supercritical when $\mathscr{R}$ is sufficiently small, but switch to subcritical as $\mathscr{R}$ is increased. Hexagons bifurcate transcritically, but with very shallow subcritical turning points for small $\mathscr{R}$. When $\mathscr{R}$ is increased, the bifurcation for the hexagons changes direction, and they become essentially subcritical. So, in general, increasing the flow amplitude favors subcritical instability for all types of solutions examined.

In general, we found that the flow has little impact on the system when the frequency and Schmidt number are in the destabilizing range. Clearly, this is an effect of the weak-flow limit, as microstructure will be significantly altered by a stronger version of this flow any time the interface remains unstable in its presence. The steady rolls, squares and hexagons indicated by the analysis of this chapter are leading-order approximations for the interface shape in a specific limit. Higher-order corrections to the evolution equation would indicate time-periodic variations of these patterns as one moves vertically through the crystal, and a large amplitude flow would likely render the patterns unrecognizable.

When the flow parameters are in the stabilizing range, we found that the bifurcation structure for all types of solutions (rolls, squares, hexagons and mixed modes) changes only in scale until a critical value of $\mathscr{R}$ is surpassed. Beyond these transition points, which are distinct for each solution type, bifurcations switch from super- to subcritical. In general, lowering the frequency Ω lowers these transitions, and increasing the frequency raises them.

ACKNOWLEDGMENTS

APPENDIX: DETAILS OF DERIVATION OF EVOLUTION EQUATION

The nonzero solutions for the lower-order terms appearing in the expansions (20) are given below. The solution for $\mathbf{u}_2$ requires a boundary layer solution so that it may satisfy the far-field conditions. The boundary layer equations are rescaled using an outer vertical coordinate $\eta = \epsilon^2 \zeta$. The resulting boundary layer solution, indicated below with an "o" superscript, gives rise to the nonlocal behavior of the flow-term in the evolution equation. Other solutions are divided into portions which are steady with respect to the fast time scale and portions which are periodic in the fast time scale with the same period as the external forcing. In these

cases we decompose each of the dependent variables into these two types of terms; for example $\phi(X,Y,T,\zeta,\tau)$ would be given as

$$\phi(X,Y,T,\zeta,\tau) = \overline{\phi}(X,Y,T,\zeta) + [\widetilde{\phi}(X,Y,T,\zeta)e^{i\tau} + \text{c.c.}],$$
(A1)

where the bar indicates the steady portion and the tilde indicates the coefficient of the $e^{i\tau}$ terms. Terms with periods other than that of the external forcing have been omitted, for they do not play a role in the analysis:

$$\mathbf{u}_0 = [\mathbf{r}(e^{-s_0\zeta} - 1)e^{i\tau} + \text{c.c.}],$$
(A2a)

$$C_0 = 1 - e^{-\zeta},$$
(A2b)

$$w_2 = \nabla h_0 \cdot \mathbf{u}_0,$$
(A2c)

$$\mathbf{u}_2 = \nabla \mathbf{a}_0 \cdot [\mathbf{r}(e^{-s_0\zeta} - 1)e^{i\tau} + \text{c.c.}] = \nabla \mathbf{a}_0 \cdot \mathbf{u}_0,$$
(A2d)

$$\hat{\mathbf{u}}_2^o = -\frac{\mathbf{k}\mathbf{k}}{|\mathbf{k}|} \cdot (\mathbf{r}e^{i\tau} + \text{c.c.})e^{-|\mathbf{k}|\eta}\hat{h}_0,$$
(A2e)

$$C_4 = -e^{-\zeta}\nabla^2 h_0/k + (\Omega h_{0T} - \nabla^2 h_0 - |\nabla h_0|^2)\zeta e^{-\zeta},$$
(A2f)

$$C_5 = \mathscr{R}[\mathbf{r}(b_0 e^{-s_2\zeta} + b_1 e^{-\zeta} + b_2 e^{-(s_0+1)\zeta} + b_3\zeta e^{-\zeta})e^{i\tau}$$
$$+ \text{c.c.}] \cdot \nabla^2 \mathbf{a}_0,$$
(A2g)

$$h_5 = \mathscr{R}(\mathbf{r}\widetilde{h}_5 e^{i\tau} + \text{c.c.}),$$
(A2h)

$$\widetilde{h}_5 = \frac{1}{s_2 - 1 - i\Omega}\left[(s_0 - s_2 + 1)b_2 - b_3 + (s_2 - 1)\right.$$
$$\left. \times \left(\frac{b_3}{(i\Omega)} + \frac{i}{s_0\Omega}\right)\right],$$
(A2i)

$$\overline{\mathbf{u}}_5 = \mathscr{R}[a_1 e^{-\zeta/S} + a_2 e^{-s_0\zeta} + a_3 e^{-s_0^*\zeta} + a_4 e^{-(s_0+s_0^*)\zeta}$$
$$+ a_5\zeta e^{-s_0\zeta} + \text{c.c.}]|\mathbf{r}\cdot\nabla|^2\mathbf{a}_0,$$
(A2j)

where the caret indicates the Fourier transform of a quantity (see below) and the notation "$\mathbf{k}\mathbf{k}$" indicates a dyadic product. The coefficients appearing in these equation are given by

$$\mathbf{r} = \frac{1}{2}(\mathbf{i} + \beta e^{-i\gamma}\mathbf{j}),$$
(A3)

$$s_0 = \frac{1}{2S}[1 + (1 + 4iS\Omega)^{1/2}],$$
(A4)

$$s_2 = [1 + (1 + 4i\Omega)^{1/2}]/2,$$
(A5)

$$\mathbf{a}_0 = \mathscr{F}^{-1}\left[\frac{i\mathbf{k}\hat{h}_0}{|\mathbf{k}|}\right],$$
(A6)

$$b_0 = -(b_1 + b_2),$$
(A7)

$$b_1 = \widetilde{h}_5 - \frac{i}{s_0\Omega} + \frac{ib_3}{\Omega},$$
(A8)

$$b_2 = \frac{1}{s_0[s_0^2 + s_0 - i\Omega]},$$
(A9)

$$b_3 = \frac{i}{\Omega},$$
(A10)

$$a_1 = -(a_2 + a_3 + a_4 + \text{c.c.})/2,$$
(A11)

$$a_2 = \frac{s_0/s_0^* - 1 + a_5(2Ss_0 - 1)}{s_0^2 S - s_0},$$
(A12)

$$a_3 = \frac{i\Omega\widetilde{h}_5 s_0^* - 1}{Ss_0^{*2} - s_0^*},$$
(A13)

$$a_4 = \frac{s_0/s_0^* - 1}{s_0 + s_0^* - S(s_0 + s_0^*)^2},$$
(A14)

$$a_5 = \frac{1}{1 - s_0 S},$$
(A15)

where $\mathbf{r}$ is given by equation (7) and $\mathscr{F}^{-1}$ indicates the inverse of the double Fourier transform in the slow scales X and Y:

$$\mathscr{F}[\phi(X,Y,T,\tau,\eta)] = \hat{\phi}(k_1,k_2,T,\tau,\eta)$$
$$= \frac{1}{2\pi}\int_{-\infty}^{\infty}\int_{-\infty}^{\infty}\phi e^{i\mathbf{k}\cdot\mathbf{X}}dXdY. \quad \text{(A16)}$$

Here $\mathbf{k} = (k_1, k_2)$ and $\mathbf{X} = (X, Y)$.

The coefficient f_0 in equation (23) is given by

$$f_0 = \frac{a_1}{S^{-1} + 1} + \frac{a_2}{s_0 + 1} + \frac{a_3}{s_0^* + 1} + \frac{a_4}{s_0 + s_0^* + 1} + \frac{a_5}{(s_0 + 1)^2}$$
$$+ \frac{b_0 s_0^*}{s_2(s_2 + s_0^*)} + \frac{b_1 s_0^*}{s_0^* + 1} + \frac{b_2 s_0^*}{(s_0 + 1)(s_0^* + s_0 + 1)}$$
$$+ \frac{b_3(s_0^{*2} + 2s_0^*)}{[s_0^* + 1]^2} + \text{c.c.} \quad \text{(A17)}$$

[1] W. A. Tiller, K. A. Jackson, J. W. Rutter, and B. Chalmers, "The redistribution of solute atoms during the solidification of metals," Acta Metall. **1**, 428 (1953).

[2] W. W. Mullins and R. F. Sekerka, "Stability of a planar interface during the solidification of a binary alloy," J. Appl. Phys. **35**, 444 (1964).

[3] S. H. Davis, in *Handbook of Crystal Growth*, edited by D. T. J. Hurle (North-Holland, Amsterdam, 1993), p. 859.

[4] T. P. Schulze and S. H. Davis, "The influence of oscillatory and steady shears on interfacial stability during directional solidification," J. Cryst. Growth **143**, 317 (1994).

[5] T. P. Schulze and S. H. Davis, "Shear stabilization of morphological instability during directional solidification," J. Cryst. Growth **149**, 253 (1995).

[6] R. E. Kelly and H. -C. Hu, "The onset of Rayleigh-Benard convection in nonplanar oscillatory flows," J. Fluid Mech. **249**, 373 (1993).

[7] D. J. Wollkind and L. A. Segel, "A nonlinear stability analysis of the freezing of a dilute binary alloy," Philos. Trans. R. Soc. London Ser. A **268**, 351 (1970).

[8] G. I. Sivashinsky, "On cellular instability in the solidification of a dilute binary alloy," Physica D **8**, 243 (1983).

[9] D. S. Riley and S. H. Davis, "Long-wave interactions in morphological and convective instabilities in the directional solidification of a dilute binary alloy," SIAM J. Appl. Math. **50**, 420 (1990).

[10] K. Brattkus and S. H. Davis, "Cellular growth near absolute stability," Phys. Rev. B **38**, 11452 (1988).

[11] A. K. Hobbs and P. Metzener, "Directional solidification: Interface dynamics and weak remote flow," J. Cryst. Growth **118**, 319 (1992).

[12] K. Kassner, C. Misbah, H. Muller-Krumbhaar, and A. Valance, "Directional solidification at high speed. 1. Secondary instabilities," Phys. Rev. E **49**, 5477 (1994).

[13] K. Kassner, C. Misbah, H. Muller-Krumbhaar, and A. Valance, "Directional solidification at high speed. 2. Transition to chaos," Phys. Rev. E **49**, 5495 (1994).

[14] W. Kurz and R. Trivedi, ''Solidification microstructures—Recent developments and future directions,'' Acta Metall. Mat. **38**, 1 (1990).

[15] S. R. Coriell and R. F. Sekerka, ''Oscillatory morphological instabilities due to non-equilibrium segregation,'' J. Cryst. Growth **61**, 499 (1983).

[16] G. J. Merchant and S. H. Davis, ''Morphological instability in rapid directional solidification,'' Acta. Metall. Mat. **38**, 2683 (1990).

[17] D. A. Huntley and S. H. Davis, ''Thermal effects in rapid directional solidification—Linear-theory,'' Acta. Metall. Mat. **41**, 2025 (1993).

[18] D. A. Huntley and S. H. Davis, ''Thermal effects in rapid directional solidification—Weakly-nonlinear analysis of oscillatory instabilities,'' J. Cryst. Growth **132**, 141 (1993).

[19] R. B Hoyle, G. B. McFadden, and S. H. Davis, ''Pattern selection with anisotropy during directional solidification,'' Philos. Trans. R. Soc. (in press).

[20] J. S. Langer, ''Instabilities and pattern formation in crystal growth,'' Rev. Mod. Phys. **52**, 1 (1980).

[21] L. R. Morris and W. C. Winegard, ''The development of cells during the solidification of a dilute Pb-Sn alloy,'' J. Cryst. Growth **5**, 361 (1969).

[22] T. P. Schulze, ''Shear stabilization of morphological instability during directional solidification,'' Ph.D. thesis, Department of Engineering Sciences and Applied Mathematics, Northwestern University, 1995.

[23] A. C. Skeldon, G. B. McFadden, M. D. Impey, D. S. Riley, K. A. Cliffe, A. A. Wheeler, and S. H. Davis, ''On long-wave morphological instabilities in directional solidification,'' Eur. J. Appl. Math. **6**, 1 (1995).